bioRχiv

ESCRT disruption provides evidence against signaling functions for synaptic exosomes

Erica C. Dresselhaus[1], Kathryn P. Harris[2], Kate Koles[1], Matthew F. Pescosolido[1], Biljana Ermanoska[1], Mark Rozencwaig[1], Rebecca C. Soslowsky[1], Bryan A. Stewart[3], Avital A. Rodal[1,*]
[1] Department of Biology, Brandeis University, Waltham, MA
[2] Office of the Vice-Principal, Research, University of Toronto, Mississauga, Mississauga, Canada
[3] Department of Biology, University of Toronto Mississauga, Mississauga, Canada; Department of Cell and Systems Biology University of Toronto, Toronto, Canada

*Corresponding author:
Email: arodal@brandeis.edu

Key words: ESCRT, Tsg101, Hrs, Shrub, Vps4, Amyloid Precursor Protein, Synaptotagmin-4, Neuroglian, Evi, Wingless, *Drosophila*, extracellular vesicle, endosome, exosome, synapse

Exosomes are membrane-bound vesicles released by many cells including neurons, carrying cargoes involved in signaling and disease. It has been unclear whether exosomes promote intercellular signaling *in vivo* or serve primarily to dispose of unwanted cargo. This is because manipulations of exosome cargo expression or traffic often result in their depletion from the donor cell, making it difficult to distinguish whether these cargoes act cell-autonomously or through transcellular transfer. Exosomes arise when multivesicular endosomes fuse with the plasma membrane, releasing their intralumenal vesicles outside the cell. We show that loss of multivesicular endosome-generating ESCRT (endosomal sorting complex required for transport) machinery disrupts release of exosome cargoes from *Drosophila* motor neurons, without depleting them from the donor presynaptic terminal. Cargoes and autophagic vacuoles accumulate in presynaptic terminals, suggesting that compensatory autophagy follows endosome dysfunction. Surprisingly, exosome cargoes Synaptotagmin-4 (Syt4) and Evenness Interrupted (Evi) retain many of their signaling activities upon ESCRT depletion, despite being trapped in presynaptic terminals. Thus, these cargoes may not require intercellular transfer, and instead are likely to function cell autonomously in the motor neuron. Our results indicate that synaptic exosome release depends on ESCRT, and serves primarily as a proteostatic mechanism for at least some cargoes.

Introduction

Neurons release extracellular vesicles (EVs) that can mediate intercellular communication, dispose of unwanted neuronal components, and propagate pathological factors in neurodegenerative disease (Budnik et al., 2016; Holm et al., 2018; Song et al., 2020). Many elegant functional studies of neuronal EVs involve their purification from donor cells and subsequent application to target cells for tests of biological activity (e.g. Gong et al., 2016; Vilcaes et al., 2021). These experiments demonstrate that EVs containing specific cargoes are sufficient to cause functional changes in the recipient cell, but do not rigorously show that traffic into EVs is necessary for the functions of cargoes *in vivo*. In the donor cell, EV cargoes are typically trafficked through the secretory system, plasma membrane, and endosomal network, where they might execute intracellular activities before being released (van Niel et al., 2018). Therefore, to test the physiological functions of EVs *in vivo*, it will be essential to uncouple potential donor cell-autonomous from transcellular functions of these cargoes, using tools that specifically block EV release. Developing such tools will require a deeper understanding of how cargoes are packaged into EVs, and released in a spatially and temporally controlled fashion, especially within the complex morphology of neurons (Blanchette and Rodal, 2020).

Exosomes are a type of EV that arise when multivesicular endosomes (MVEs) fuse with the plasma membrane, releasing their intralumenal vesicles (ILVs) into the extracellular space. Spatial and temporal regulation of the machinery that controls formation of MVEs is therefore likely to be critical for exosome cargo selection, packaging, and release. MVEs can form via multiple nonexclusive mechanisms for budding of vesicles into the endosomal lumen (van Niel et al., 2018). One such pathway relies on Endosomal Sorting Complex Required for Traffic (ESCRT) proteins. In this pathway, ESCRT-0, -I, and -II components cluster cargoes, deform membranes, and then recruit ESCRT-III components, which form a helical polymer that drives fission of the ILV. Finally, the VPS4 ATPase recycles ESCRT-III filaments (Gruenberg, 2020; Vietri et al., 2020). The ESCRT-I component Tsg101 (Tumor susceptibility gene 101) is incorporated into and serves as a common marker for EVs, highlighting the link between ESCRT and EVs (van Niel et al., 2018). A neutral sphingomyelinase (nSMase)-mediated pathway may operate together with or in parallel to ESCRT to generate EVs by directly modifying lipids and altering their curvature, and indeed EV release of many neuronal cargoes is sensitive to nSMase depletion or inhibition (Asai et al., 2015; Dinkins et al., 2016; Goncalves et al., 2015; Guo et al., 2015; Men et al., 2019; Sackmann et al., 2019). The

ESCRT machinery also has functions beyond MVE formation, including autophagosome closure and organelle repair, which are in turn involved in alternative modes of EV biogenesis (Arbo et al., 2020; Lefebvre et al., 2018; Leidal and Debnath, 2021; Moreau et al., 2013; Zhen and Stenmark, 2023). However, there is evidence both for and against a role for ESCRT in EV biogenesis in different neuronal cell types (Cone et al., 2020; Coulter et al., 2018; Gong et al., 2016). Thus, it remains unclear if or how EV dysfunction contributes to organism-level physiological defects resulting from ESCRT disruption, including ESCRT-linked human neurological disease (Dubey et al., 2022; Filimonenko et al., 2007; Ugbode and West, 2021; Willén et al., 2017; Yan and Zheng, 2021).

At the *Drosophila* larval neuromuscular junction (NMJ), EVs are released from presynaptic motor neurons into extrasynaptic space within the muscle membrane subsynaptic reticulum, and can also be taken up by muscles and glia (Fuentes-Medel et al., 2009; Koles et al., 2012). These EVs are likely to be exosomes, as cargoes are found in presynaptic MVEs, and depend on endosomal sorting machinery for their release and regulation (Blanchette et al., 2022; Koles et al., 2012; Korkut et al., 2009; Lauwers et al., 2018; Walsh et al., 2021). This system provides the powerful advantage of investigating endogenous or exogenous exosome cargoes with known physiological functions in their normal tissue and developmental context. Cargoes characterized to date include Synaptotagmin-4 (Syt4, which mediates functional and structural plasticity), Amyloid Precursor Protein (APP, a signaling protein involved in Alzheimer's Disease), Evenness Interrupted/Wntless/Sprinter (Evi, which carries Wnt/Wingless (Wg) to regulate synaptic development and plasticity), and Neuroglian (Nrg, a cell adhesion molecule) (Korkut et al., 2013, 2009; Walsh et al., 2021). Mutants in trafficking machinery (for example *evi* and the recycling endosome GTPase *rab11*) cause reduced levels of cargo in EVs and show defects in EV cargo physiological activities, leading to the hypothesis that trans-synaptic transfer of these cargoes into the postsynaptic muscle is required for their signaling functions (Budnik et al., 2016). However, we and others have shown that these mutants also have a dramatic local presynaptic decrease in cargo levels, making it difficult to rule the donor neuron out as their site of action (Ashley et al., 2018; Blanchette et al., 2022; Koles et al., 2012; Korkut et al., 2009; Walsh et al., 2021). Here we show that disruption of the ESCRT machinery causes a specific loss of EV release without depleting presynaptic cargo levels, and use this system to test whether exosome release is required for cargo signaling functions.

Results

ESCRT machinery promotes EV release from synapses

To determine if the ESCRT pathway is involved in EV release at the *Drosophila* NMJ synapse, we first used GAL4/UAS-driven RNAi to knock down the ESCRT-I component Tsg101 (Tumor susceptibility gene 101) specifically in neurons ($Tsg101^{KD}$). We then used our previously established methods to measure the levels of the endogenously tagged EV cargo Syt4-GFP, both in the donor presynaptic compartment and in neuron-derived EVs in the adjacent postsynaptic cleft and muscle (Walsh et al., 2021). Neuronal knockdown of Tsg101 ($Tsg101^{KD}$) led to accumulation of Syt4-GFP in the presynaptic compartment, together with a striking loss of postsynaptic Syt4-GFP EVs (**Fig 1A, E**). We next tested the effects of $Tsg101^{KD}$ on three other known EV cargoes: UAS-driven Evi-GFP **(1B, F)** or human APP-GFP **(1C, G)**, and endogenous Nrg **(1D, H)** (Korkut et al., 2013, 2009; Walsh et al., 2021). For all three cargoes, we observed a similar phenotype as seen for Syt4-GFP: presynaptic redistribution in large structures (accumulating to particularly high levels for Syt4-GFP and Evi-GFP), together with loss of postsynaptic EV signal. Thus, multiple EV cargoes, either endogenously or exogenously expressed, require the ESCRT-I component Tsg101 for release in neuronally-derived EVs. Further, since cargoes accumulate in internal structures upon $Tsg101^{KD}$, these data suggest that NMJ EVs are derived from intracellular MVEs rather than budding directly from the plasma membrane, so we will refer to them as exosomes for the remainder of this study.

In addition to its functions in MVE biogenesis, Tsg101 also plays roles in numerous cellular processes including membrane repair, lipid transfer, neurite pruning, and autophagy, each depending on a specific subset of other ESCRT machinery (Vietri et al., 2020). We therefore tested if exosome release depends on other canonical ESCRT components. Hrs (Hepatocyte growth factor receptor substrate) is a component of the ESCRT-0 complex and is required to cluster exosome cargo on the delimiting membrane of the endosome (Vietri et al., 2020). Similar to $Tsg101^{KD}$, *Hrs* loss-of-function mutants caused a drastic decrease in postsynaptic Nrg, though interestingly presynaptic Nrg was also partially depleted, unlike the $Tsg101^{KD}$ condition (**Fig 1I, J**). Next, we tested ESCRT-III, which forms the polymer involved in constriction and scission of the ILV neck. The *Drosophila* genome encodes several ESCRT-III proteins, of which *shrub* is homologous to mammalian CHMP4B. Shrub is likely to play an important role at synapses, since its loss leads to defects in NMJ morphogenesis and ILV formation (Sweeney et al., 2006). Pan-neuronal RNAi of *shrub* ($Shrub^{KD}$) caused a dramatic loss of postsynaptic Syt4 and Nrg signals (**Fig. 1K-M**). Finally, we examined the role of Vps4, which catalyzes disassembly of the ESCRT-III polymer, finalizing the formation of the ILV. Pan-neuronal expression of a dominant negative Vps4 fragment ($Vps4^{DN}$, (Rodahl et al., 2009)) strongly reduced postsynaptic levels of both Syt4-GFP and Nrg, and increased their presynaptic levels (**Fig. 1N-P**). These results demonstrate that multiple components of the ESCRT pathway are required for release of exosome cargoes at neuronal synapses, with variable effects on presynaptic accumulation of these cargoes.

Loss of Tsg101 leads to accumulation of cargoes in arrested autophagic structures

To explore the nature of the presynaptic accumulations of exosome cargoes at $Tsg101^{KD}$ NMJs, we examined their colocalization with early (Rab5) and recycling (Rab11) endosomes, which drive an endosome-to-plasma membrane recycling flux that supplies the exosome biogenesis pathway at this synapse (Korkut 2009, 2014,

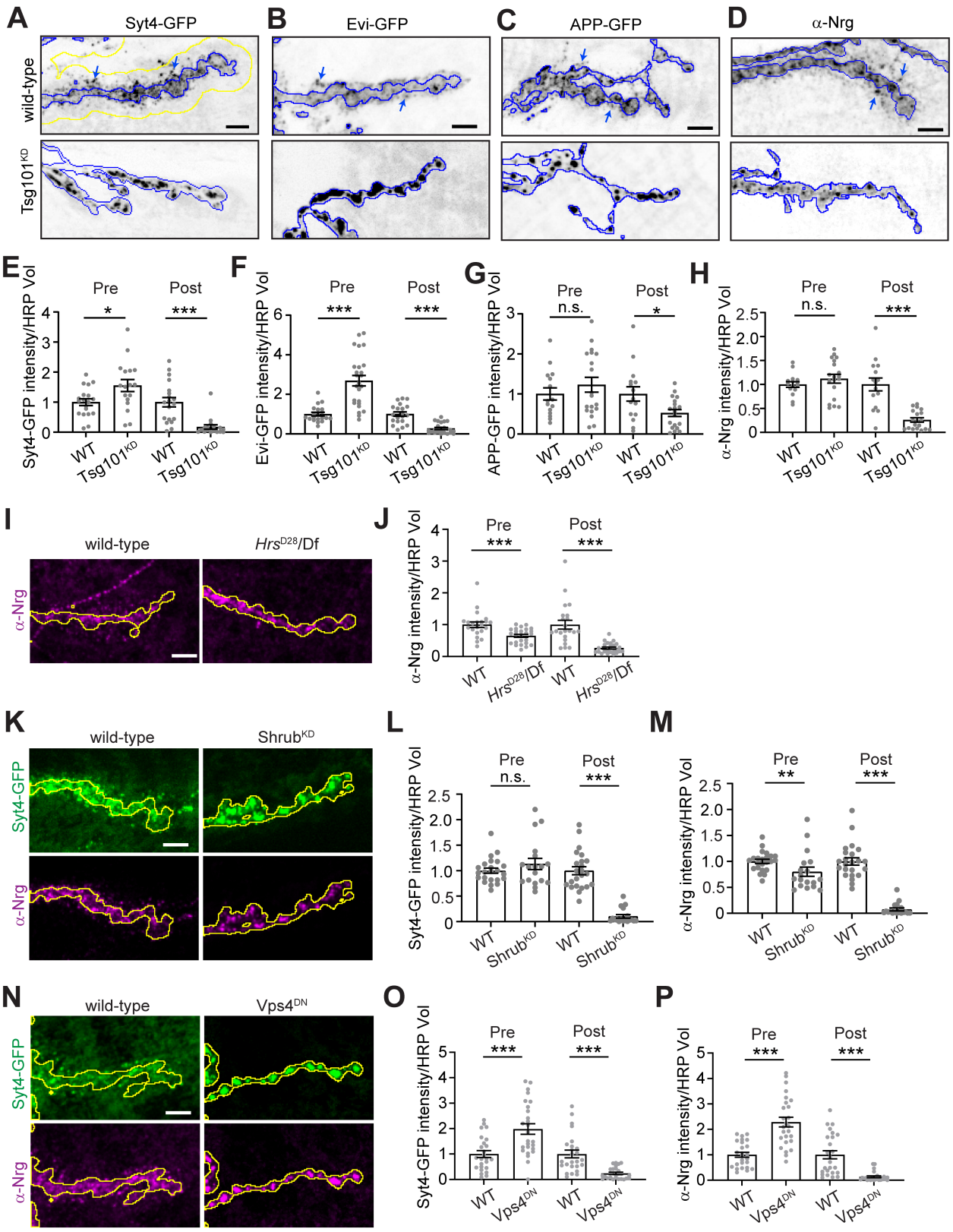

Fig 1. ESCRT complex is required for the release of EV cargoes from presynaptic terminals. **(A-D)** Representative confocal images from larvae expressing UAS-Tsg101-RNAi (Tsg101^{KD}) either pan-neuronally (C380-GAL4) or in motor neurons (Vglut-GAL4) together with the following EV cargoes: **(A)** Syt4-GFP expressed from its endogenous locus, **(B)** UAS-driven Evi-GFP, **(C)** UAS-driven APP-GFP, **(D)** endogenous neuroglian (Nrg, neuronal isoform Nrg180) detected by antibody. **(E-H)** Quantification of normalized EV cargo puncta intensity. **(I)** Representative confocal images from *Hrs* mutant larvae, labeled with α-Nrg antibody. **(J)** Quantification of normalized Nrg puncta intensity. **(K)** Representative confocal images of endogenously tagged Syt4-GFP and α-Nrg in larvae pan-neuronally expressing UAS-Shrub-RNAi (Shrub^{KD}). **(L-M)** Quantification of normalized Syt4-GFP and Nrg puncta intensity. **(N)** Representative confocal images of endogenously tagged Syt4-GFP and α-Nrg from larvae expressing UAS-Vps4^{DN} pan-neuronally. **(O-P)** Quantification of normalized Syt4-GFP and Nrg puncta intensity.
All scale bars = 5 μm. **(A-D)** Blue outlines represent the neuronal membrane as marked from an HRP mask and yellow line represent a 3 μm dilation of HRP mask, representing the postsynaptic region. (**I, K, N**) Yellow outline represents the neuronal membrane as marked from an HRP mask. Data is represented as mean +/- s.e.m.; n represents NMJs. Arrows show examples of postsynaptic EVs. All values are normalized to their respective controls. *p<0.05, **p<0.01, ***p<0.001. **See Tables S1 and S3 for detailed genotypes and statistical analyses.**

Walsh 2021). We also examined cargo co-localization with late endosomes (Rab7), which play less important roles in NMJ exosome traffic (Walsh 2021). We found that exosome cargoes exhibited increased co-localization with all these endosomal markers at Tsg101^{KD} synapses, in what appeared to be multi-endosome clusters (**Fig 2A, S1A-C**). These results argue against formation of a single type of arrested MVE such as the canonical Class E compartment in ESCRT-deficient yeast and mammalian cells (Doyotte et al., 2005; Raymond et al., 1992) and instead suggest a more global defect in endosome maturation or turnover. To test this hypothesis, we measured the overall mean intensity as well as puncta number and size for Rab5, Rab7, and Rab11 upon Tsg101 knockdown. We saw no changes in the total intensity or puncta parameters for Rab7 (**Fig S1D-F**). However, for both Rab5 and Rab11, we observed a significant increase in Rab puncta intensity, mean intensity over the whole NMJ, and an increase in puncta size, with no change (Rab11) or a slight decrease (Rab5) in the number of puncta (**Fig S1D-F)**. These results suggest defects in early and recycling endosome maturation and/or turnover upon loss of ESCRT function.

We next examined Tsg101^{KD} NMJs using transmission electron microscopy (TEM). Tsg101^{KD} boutons retained typical mitochondria, synaptic vesicles and active zone "T-bars", and were surrounded by an apparently normal subsynaptic reticulum, representing the infolded postsynaptic muscle membrane. However, within Tsg101^{KD} boutons we observed striking clusters of double membrane-surrounded or electron-dense structures, typical of autophagic vacuoles at various stages of maturation (Klionsky et al., 2021), including those with unclosed phagophores (**Fig. 2B**; three or more autophagic vacuoles were observed in 58.9% of mutant boutons (n=56) compared to 2.5% of control boutons (n=40), $p<0.0001$). Given that secretion of autophagosomal contents has been described as an EV-generating mechanism (Buratta et al., 2020), we next tested whether core autophagy machinery might play a role in exosome release at the *Drosophila* NMJ, and could therefore be linked to the Tsg101^{KD} exosome phenotype. Atg1 is a kinase that is required for the initiation of phagophore assembly, and acts as a scaffold for recruitment of subsequent proteins, while Atg2 is required for phospholipid transfer to the phagophore (Nakatogawa, 2020). We observed a modest but significant decrease in both pre- and post-synaptic levels of the exosome marker Nrg upon disruption of autophagy by RNAi-mediated knockdown of Atg1 (knockdown validated in **Fig. S2A**, Nrg results in **Fig. S2B-C**), as well as by loss-of-function *Atg2* mutations (**Fig. S2D-E**). Notably, these mutants did not recapitulate the ESCRT mutant phenotype of dramatic depletion of postsynaptic exosomes and presynaptically trapped cargoes. These results indicate that autophagic machinery does not play a major role in exosome biogenesis or release at the NMJ, and that the autophagic defects at Tsg101^{KD} NMJs are likely separable from its roles in exosome release.

To further explore these autophagic defects, we next used the reporter GFP-mCherry-Atg8/LC3 to assess autophagic flux in Tsg101^{KD} neurons. Under normal circumstances, the GFP moiety in this reporter is quenched when autophagosomes fuse with acidic endosomes and lysosomes, while mCherry retains its fluorescence. By contrast, defects in autophagic flux lead to accumulation of structures with both GFP and mCherry fluorescence (Klionsky et al., 2021). We examined this flux in motor neuron cell bodies, where mature autolysosomes are predicted to accumulate (Sidibe et al., 2022). In wild-type animals we observed mCherry-positive/GFP-negative puncta reflecting mature autolysosomes. By contrast we observed an increased volume of intense puncta in the cell bodies of Tsg101^{KD} motor neurons, most of which were labeled by both mCherry and GFP (**Fig. 2C, D, S2F**). These data suggest that Tsg101^{KD} causes a defect in autophagic flux.

Since autophagy is normally rare at wild-type *Drosophila* NMJ synapses (Soukup et al., 2016), we hypothesized that ESCRT mutants might activate a compensatory "endosomophagy" pathway to degrade ESCRT-deficient endosomes (Millarte et al., 2022). However, since Tsg101 is also required for phagophore closure (Takahashi et al., 2019), this process is likely unable to dispose of defective endosomes upon Tsg101 knockdown. By contrast, ESCRT-0/Hrs is not required for autophagy in some cell types, such as *Drosophila* fat body (Rusten et al., 2007). To test if this also applies to motor neurons, we examined GFP-mCherry-Atg8 in *Hrs* mutant motor neuron cell bodies, and found mCherry-positive, GFP-negative structures, similar to controls (**Fig. 2C, E**), suggesting that Hrs is not required for autophagic flux in motor neurons. Interestingly, we did observe an increase in the area covered by puncta, indicating that autophagy is induced in *Hrs* mutants (**Fig. 2C**). Overall, given that *Tsg101* and *Hrs* have different autophagy phenotypes but similar EV release defects, our results suggest that autophagy and EV traffic are separable functions of ESCRT at the synapse, and that a compensatory (and Tsg101-dependent) autophagy mechanism might be activated to remove defective endosomes in *Hrs* mutants.

Finally, we further explored whether accumulation of EV cargoes in arrested structures was local to the synapse or occurring throughout the neuron. First, we examined Syt4-GFP levels in motor neuron cell bodies and axons after Tsg101 knockdown, and found that Syt4-GFP accumulated significantly at both locations (**Fig. 2F-I**). To ask whether the presynaptic accumulations could be due to faster anterograde or slowed retrograde transport of exosome cargo-containing compartments, we next conducted live imaging and kymograph analysis of motor neuron-driven APP-GFP, as well as a mitochondrial marker. We found that Tsg101 knockdown led to a large increase in the number of stationary APP-GFP puncta in axons without affecting the number of compartments undergoing retrograde or anterograde transport (**Fig S3A,B**), though we observed a small decrease in the retrograde transport rate (**Fig S3C**). By contrast, we did not observe an increase in the steady state intensity of the mitochondrial marker or see any changes in its transport behavior (**Fig S3D-H**), suggesting that axonal accumulations are specific to exosome cargo.

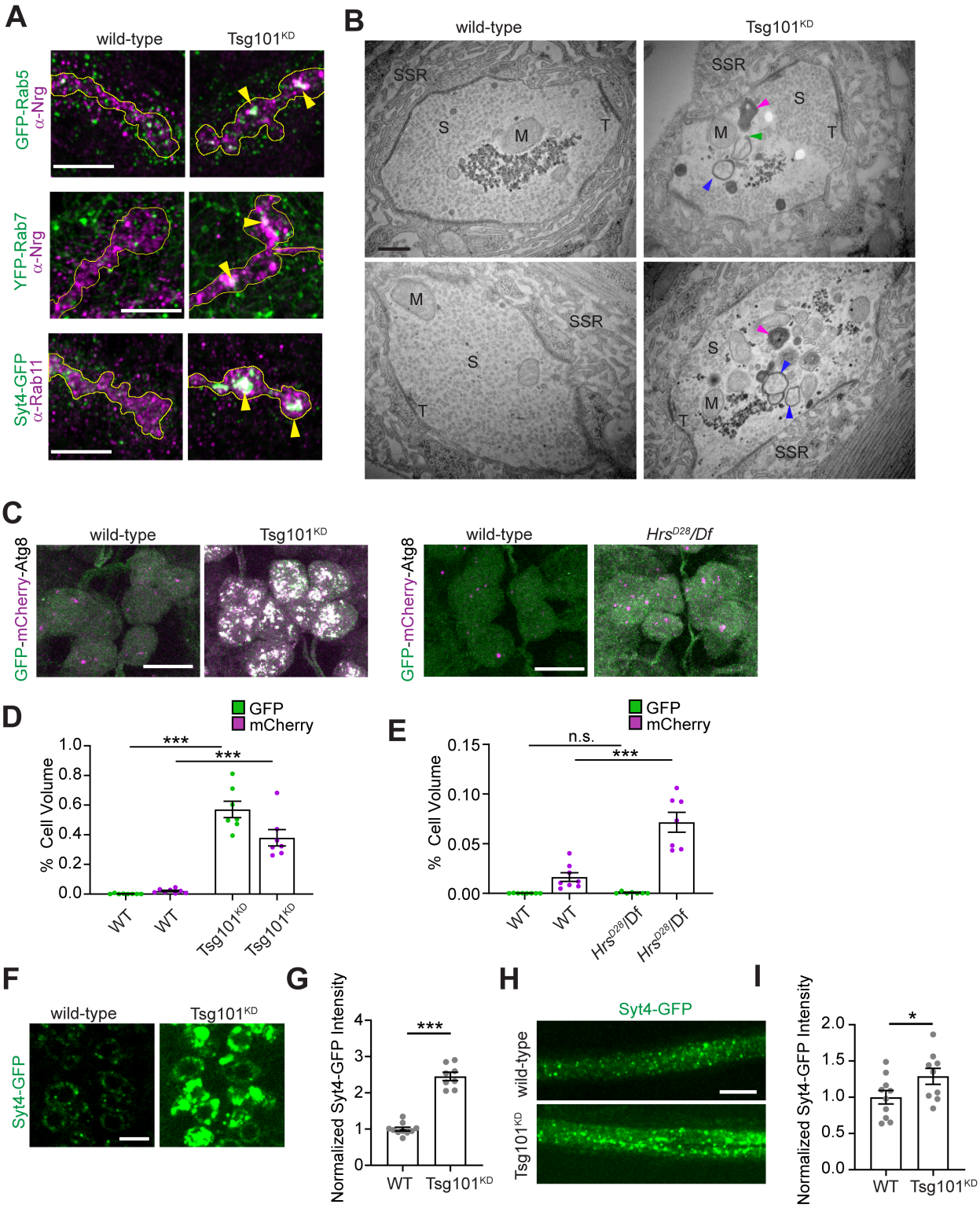

Figure 2: Synaptic EV cargoes accumulate in abnormal endosomal and autophagic structures upon neuronal Tsg101 knockdown. (A) Representative Airyscan images showing co-localization of EV cargoes Syt4-GFP or α-Nrg with endosomal markers α-Rab11, GFP-Rab5 (endogenous tag), or YFP-Rab7 (endogenous tag). Scale bar = 5 μm. **(B)** Representative transmission electron microscopy images of boutons from muscle 6/7 from wild-type and neuronal Tsg101^{KD} larvae. Examples of autophagic vacuoles are marked with arrowheads, blue = autophagosome, magenta = autolysosome, and green = unclosed phagophore. Other notable features include T = T-bar, S = synaptic vesicles, M = mitochondria, SSR = subsynaptic reticulum. Scale bar = 400 nm. **(C)** Representative images from neuronal cell bodies in the ventral ganglion expressing motor neuron-driven GFP-mCherry-Atg8. Scale bar = 10 μm. Brightness/contrast were adjusted separately for each mutant compared to their respective wild-type (**see Table S3**). **(D-E)** Quantification of GFP-mCherry-Atg8 levels in Tsg101^{KD} (D) and *Hrs* mutant larvae (E)**. (F)** Representative confocal images of a single slice through the motor neuron cell bodies of the ventral ganglion. Scale bar = 10 μm. **(G)** Quantification of total Syt4-GFP intensity in the brain, normalized to control. **(H)** Maximum intensity projection of axon segment proximal to the ventral ganglion. Scale bar = 10 μm. **(I)** Quantification of total Syt4-GFP intensity in the axon, normalized to control.
Data is represented as mean +/- s.e.m.; n represents animals. Outlines represent the neuronal membrane as marked from an HRP mask. *p<0.05, ***p<0.001. **See Tables S1 and S3 for detailed genotypes and statistical analyses.**

Thus, loss of *tsg101* leads to accumulation of stationary exosome cargo-containing compartments throughout the neuron, without affecting the transport rates of moving cargoes, suggesting that altered axonal transport kinetics do not underlie synaptic accumulation.

Tsg101 knockdown does not recapitulate all *evi* or *wg* phenotypes in synaptic growth or development

Specific depletion of cargo in postsynaptic exosomes (but not the donor presynaptic terminal) upon Tsg101^{KD} provided us with a valuable tool to determine if these cargoes require trans-synaptic transfer for their known synaptic functions. Neuron-derived Wg provides anterograde (to the muscle) and paracrine (to the neuron) signals for NMJ growth, active zone development, and assembly of the postsynaptic apparatus (Miech et al., 2008; Packard et al., 2002). Evi is a multipass transmembrane protein that serves as a carrier for Wg through the secretory system, ultimately leading to its release from the cell, either by conventional exocytosis or via exosomes (Das et al., 2012). At the NMJ, Evi co-transports with Wg into exosomes, and *evi* mutants phenocopy *wg* signaling defects, providing support for the hypothesis that Evi/Wg exosomes are required for Wg signaling (Korkut et al. 2009, Koles et al. 2012). However, since Evi is broadly required for many steps of Wg traffic, *evi* mutants trap Wg in the somatodendritic compartment and prevent its transport into presynaptic terminals (Korkut et al., 2009). Therefore, Wg signaling defects in *evi* mutants may be due to generalized loss of Wg secretion rather than specific loss of its trans-synaptic transfer. *Wg* or *evi* mutants exhibit dramatic reductions in bouton number, together with the appearance of immature boutons with abnormal or missing active zones, fewer mitochondria, aberrant swellings or pockets in the postsynaptic region opposing active zones, and missing areas of PSD95/Discs-Large (DLG)-positive postsynaptic subsynaptic reticulum (Korkut et al., 2009; Packard et al., 2002). In the *evi*^{2} mutant, the number of synaptic boutons and the number of active zones (marked by ELKS/CAST/ Bruchpilot (BRP)) were both significantly reduced compared to controls, and the postsynaptic scaffolding molecule DLG frequently exhibited a "feathery" appearance, suggesting defects in postsynaptic assembly (**Fig. 3A-E**). By contrast, we found that bouton and active zone numbers at Tsg101^{KD} NMJs (which have presynaptic Evi but no Evi exosomes (**Fig. 1B**)) were not significantly different from controls. Further, active zones in Tsg101^{KD} appeared morphologically normal by TEM (**Fig. 2B**). We did not observe significant amounts of "feathery" DLG distribution in control or Tsg101^{KD} larvae (2.3% of control NMJs (n=87) and 5.5% of Tsg101KD NMJs (n=87), compared to 51.7% of *evi*^{2} mutant NMJs (n=91), p=0.27 for control versus Tsg101^{KD}). We also did not observe significant differences between control and Tsg101^{KD} NMJs in the appearance of subsynaptic reticulum by EM (**Fig. 2B**) These results indicate that some neuronal Evi and Wg functions are unexpectedly maintained despite loss of detectable postsynaptic Evi exosomes upon Tsg101^{KD}.

In addition to an overall decrease in the number of synaptic boutons, both *Wg* and *evi*^{2} mutants have been reported to show increased numbers of developmentally arrested or "ghost" boutons that feature presynaptic markers such as α-HRP antigens, but lack a postsynaptic apparatus defined by DLG (Korkut et al., 2009). We found that in *evi*^{2} mutants, these ghost boutons are more prevalent in anterior segments of the larvae, where overall synaptic growth is more exuberant. Similarly, Tsg101^{KD} animals exhibited a significant increase in ghost boutons in abdominal segment A2 (but not in A3), partially phenocopying the *evi*^{2} mutant (**Fig, 3 F,G**). To further explore this function for other ESCRT components, we quantified ghost boutons upon neuronal Shrub^{KD}. Because it was difficult to recover third instar larvae for this condition, we reared control, *evi*^{2}, Tsg101^{KD}, and Shrub^{KD} larvae at 20ºC, where RNAi expression from the neuronal GAL4 driver would be weaker. At this temperature, *evi*^{2} mutants did not show a ghost bouton phenotype, raising the possibility that this point mutant is only defective at a higher temperature (25ºC). However, both Tsg101^{KD} and Shrub^{KD} exhibited significantly increased ghost bouton number under these conditions. Taken together, these results suggest that some (but not all) aspects of subsynaptic reticulum development may require trans-synaptic transfer of Wg and Evi in exosomes.

Tsg101 knockdown does not recapitulate *syt4* phenotypes in activity-dependent structural or functional plasticity

We next explored the functions of the exosome cargo Syt4, which is required for activity-dependent structural and functional plasticity at the NMJ (Barber et al., 2009; Korkut et al., 2013; Piccioli and Littleton, 2014; Yoshihara et al., 2005). Endogenous Syt4 is thought to be generated only by the presynaptic motor neuron, based on the absence of Syt4 transcript in muscle preparations, and the finding that presynaptic RNAi of Syt4 depletes both presynaptic and postsynaptic signals (Korkut 2013). We independently verified that all the Syt4 at the NMJ was derived from the neuron, using a strain in which the endogenous Syt4 locus is tagged at its 3' end with a switchable TagRFP-T tag, which could be converted to GFP in the genome via tissue-specific GAL4/UAS expression of the Rippase recombinase (Koles et al., 2015; Walsh et al., 2021) (**Fig. S4A**). Conversion of the tag only in neurons resulted in a bright Syt4-GFP signal both presynaptically and postsynaptically, together with disappearance of the TagRFP-T signal (**Fig. S4B**). However, conversion of the tag in muscles did not result in any GFP signal, and the TagRFP-T signal remained intact. These results indicate that Syt4 is only expressed in neurons, and support the previous conclusion that the postsynaptic signal is derived from a presynaptically-expressed product (Korkut et al., 2013).

Membrane trafficking mutants such as *rab11* and *nwk* deplete Syt4 from presynaptic terminals (only secondarily reducing its traffic into exosomes), and phenocopy *syt4* null mutant plasticity phenotypes (Blanchette et al., 2022; Korkut et al., 2013; Walsh et al., 2021). However, there is no evidence to date that signaling by Syt4 explicitly requires its transfer via exosomes. We first tested the effect of Tsg101^{KD}, which depletes exosomes without diminishing presynaptic Syt4 (**Fig. 1A, E**), on Syt4- dependent structural plasticity. In

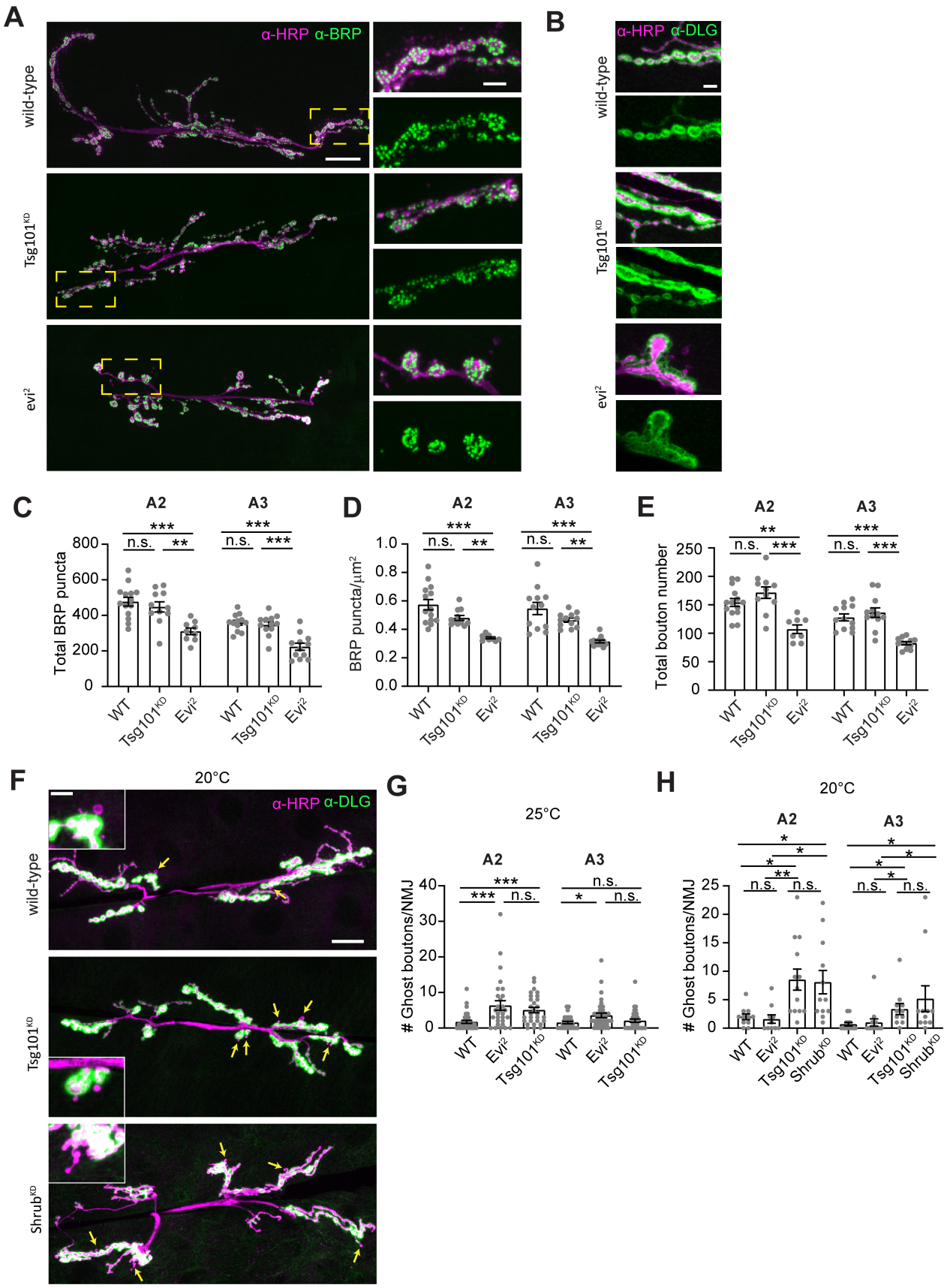

Figure 3. Tsg101^{KD} does not phenocopy all *evi* and *wg* synaptic morphology defects. **(A)** Representative confocal images of muscle 6/7 NMJ labeled with α-HRP and α-BRP antibodies (left). Magnification of the yellow boxed area (right). HRP brightness was adjusted independently. **(B)** Representative confocal images of muscle 6/7 NMJ highlighting α-DLG pattern. **(C)** Quantification of total active zone number on muscle 6/7. **(D)** Quantification of active zones per NMJ area. **(E)** Quantification of total bouton number on muscle 6/7. **(F)** Representative confocal images of muscle 6/7 NMJ labeled with α-HRP and α-DLG antibodies. Yellow arrows indicate ghost boutons. **(G)** Quantification of baseline ghost boutons from larvae cultivated at 25°C. **(H)** Quantification of baseline ghost boutons from larvae cultivated at 20°C.
Large image scale bar = 20 µm, small image scale bar = 5 µm. Data is represented as mean +/- s.e.m.; n represents NMJs. *p<0.05, **p<0.01, ***p<0.001. **See Tables S1 and S3 for detailed genotypes and statistical analyses.**

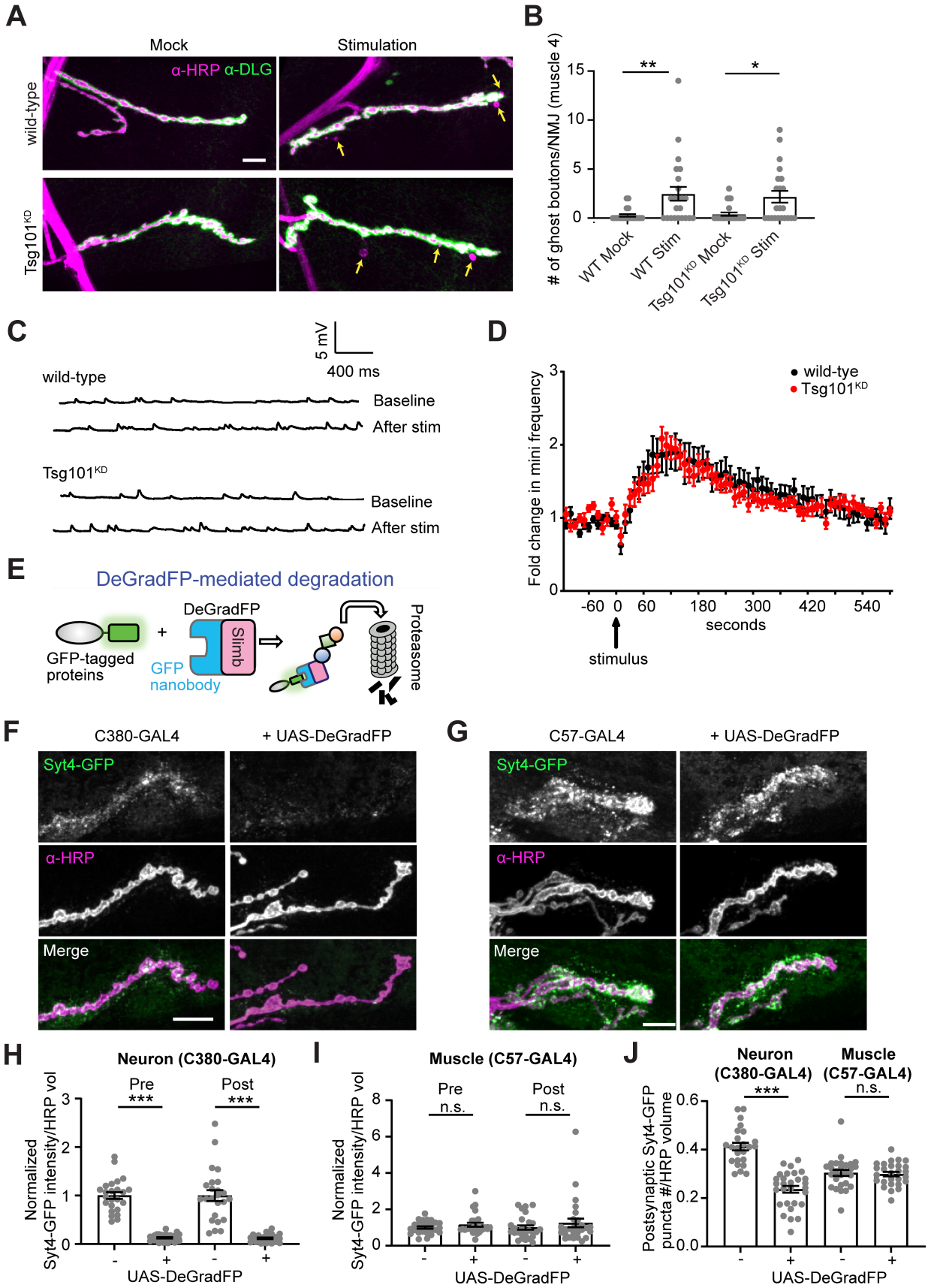

Figure 4. Tsg101^{KD} does not phenocopy *syt4* structural or functional plasticity defects, and Syt4 is not sensitive to degradation in the muscle cytoplasm. **(A)** Representative confocal images from muscle 4 in mock and spaced K^+-stimulated larvae. Arrows indicate examples of activity-dependent ghost boutons. **(B)** Quantification of ghost bouton numbers per NMJ. **(C)** Representative traces of mEJPs before (top trace) and after (bottom trace) high frequency stimulation (4 x 100 Hz). **(D)** Timecourse of mEJP frequency after stimulation. **(E)** Schematic for DeGradFP system. **(F-G)** Representative images of Syt4-GFP with neuronal (C380-GAL4, F) or muscle (C57-GAL4, G) expressed DeGradFP. **(H)** Quantification of Syt4-GFP intensity from F. **(I)** Quantification of Syt4-GFP intensity from G. **(J)** Quantification of normalized presynaptic puncta number from F and G.

All scale bars = 10 μm. Data is represented as mean +/- s.e.m.; n represents NMJs. *p<0.05, **p<0.01, ***p<0.001. **See Tables S1 and S3 for detailed genotypes and statistical analyses.**

this paradigm, spaced high potassium stimulation promotes acute formation of nascent ghost boutons (Ataman et al., 2008; Korkut et al., 2013; Piccioli and Littleton, 2014). These are likely transient structures, and thus are not directly comparable to developmentally arrested ghost boutons such as those that are found in *evi* mutants (Fernandes et al., 2021). However, to avoid the confounding presence of these immature boutons, we explored the activity-dependent synaptic growth paradigm on muscle 4, where the Tsg101^{KD} animals do not have significantly more ghost boutons than controls under baseline conditions. Unexpectedly, Tsg101^{KD} animals behaved similarly to controls, and exhibited a significant increase in ghost boutons following high K+ spaced stimulation compared to mock stimulation (**Fig. 4A-B**), suggesting that Syt4 function is preserved in these synapses despite depletion of exosomal Syt4. We were surprised by these results and contacted another laboratory (KPH, BAS) to replicate this experiment independently at muscle 6/7 in segments A3 and A4, and again saw no defect in ghost bouton formation (**Fig. S4C-D)**. KPH next tested the effect of Tsg101^{KD} on Syt4-dependent functional plasticity. In this paradigm, stimulation with 4x100 Hz pulses causes a Syt4-dependent increase in the frequency of miniature excitatory junction potentials (mEJPs), in a phenomenon termed High Frequency-Induced Miniature Release (HFMR) (Korkut et al., 2013; Yoshihara et al., 2005). Tsg101^{KD} animals exhibited similar HFMR to wild type controls, indicating that Syt4 function was not disrupted (**Fig. 4C-D**). Taken together, our results show that Syt4-dependent structural and functional plasticity at the larval NMJ can occur despite dramatic depletion of exosomal Syt4.

If trans-synaptic transfer of Syt4 in exosomes serves a calcium-responsive signaling function in the muscle, one would expect to find neuronally-derived Syt4 in the muscle cytoplasm. Conversely, if exosomes serve primarily as a proteostatic mechanism to shed neuronal Syt4 for subsequent uptake and degradation in muscles (or glia), then Syt4 would not need to be exposed to the muscle cytoplasm, as it could be taken up in double membrane compartments for degradation via fusion with muscle (or glial) lysosomes. Therefore, we tested whether neuronally-derived Syt4-GFP (for which the GFP moiety is topologically maintained on the cytoplasmic side of membranes in both donor and recipient cells) could be found in the muscle cytoplasm. Using the GAL4/UAS system, we expressed a proteasome-targeted anti-GFP nanobody (deGradFP (Caussinus et al., 2011)) only in neurons or only in muscles. We observed strong depletion of Syt4-GFP fluorescence upon presynaptic deGradFP expression, including a reduction in Syt4 postsynaptic puncta intensity and number, consistent with the presynaptic source of exosomal Syt4-GFP protein (Fig. 4F, H, J). However, we did not observe any difference in either presynaptic or postsynaptic Syt4-GFP levels or puncta number upon deGradFP expression in the muscle (Fig. 4G, I, J), though deGradFP could efficiently deplete DLG as a control postsynaptic protein (Fig. S4E). These results suggest that the majority of postsynaptic Syt4 is not exposed to the muscle cytoplasm.

Discussion

Here we show that the ESCRT pathway is required for EV cargo packaging at the *Drosophila* larval NMJ, and that these EVs are likely MVE-derived exosomes. We found that ESCRT depletion caused presynaptic accumulation of cargoes, defects in their axonal transport, and a dramatic loss of trans-synaptic transfer in exosomes. Surprisingly, we found that this trans-synaptic transfer is not required for several physiological functions of exosome cargoes Evi and Syt4. Further, neuronally-derived Syt4 could not be detected in the muscle cytoplasm, consistent with findings from Hela cells that the majority of EV cargoes remain in the endosomal system of the recipient cell (O'Brien et al., 2022). Our results suggest that neuronal exosome release for these cargoes serves primarily proteostatic and not signaling functions.

Functions of ESCRT in MVE biogenesis and exosome release at synapses

We found that ESCRT is required for exosome generation and release at the *Drosophila* larval NMJ. ESCRT components are also required for EV/exosome cargo release from primary neurons in culture (Gong et al., 2016) and Purkinje neurons *in vivo* (Coulter et al., 2018), but not for exosome release of pathogenic APP variants or Evi from cell lines (Beckett et al., 2013; Cone et al., 2020), underscoring the importance of studying membrane traffic in *bona fide* neurons. Further, we found that upon ESCRT depletion, cargoes accumulate in intracellular compartments, suggesting that this population of NMJ EVs are MVE-derived exosomes rather than plasma membrane-derived microvesicles. This is consistent with the requirement for endosomal sorting machinery, such as retromer, in their regulation (Walsh et al. 2021).

One major open question is whether exosome-precursor MVEs are generated on-demand in response to local cues at presynaptic terminals, or if they arise in response to global cues and are transported to synapses from other regions of the neuron. Answering this question will require tools to visualize the timecourse of MVE biogenesis in neurons, as have been developed in cultured non-neuronal cells (Wenzel et al., 2018). In addition, future methods (e.g. optogenetic) for acute and localized inhibition of ESCRT will reveal whether arrested structures first appear locally at the synapse and are only later transported into axons and cell bodies, and/or if they are generated far from the site of release at the synapse. These experiments will be critical for understanding when and where local or global signaling events impinge on exosome biogenesis. Interestingly, activity-dependent delivery of Hrs to presynaptic terminals is critical for proteostasis of synaptic vesicle proteins (Birdsall et al., 2022; Boecker and Holzbaur, 2019; Sheehan et al., 2016). If MVEs are generated on-demand at synapses, Hrs transport could similarly underlie the activity-dependence of exosome release, which has been reported in many (but not all) neuronal experimental systems, and remains poorly understood (Ataman et al., 2008; Fauré et al., 2006; Lachenal et al., 2011; Lee et al., 2018; Vilcaes et al., 2021).

Other synaptic functions of ESCRT

ESCRT is best-known for its functions in MVE biogenesis, but has many other potential synaptic roles including in autophagy, lipid transfer and membrane repair (Vietri et al., 2020). Our results show that the function of ESCRT in exosome release is likely separate from its roles in autophagy, since several canonical autophagy mutants do not phenocopy the exosome trafficking defects seen upon ESCRT depletion, and *Hrs* mutants exhibit exosome but not autophagic flux defects. Interestingly, we found that *atg* mutants led to an overall reduction in levels of the exosome cargo Nrg, raising the possibility that other degradative pathways are upregulated at synapses when autophagy is blocked. Tsg101 is also involved in lipid transfer to mitochondria (Wang et al., 2021), but we did not detect obvious defects in mitochondria in motor neuron axons, as were seen in *Tsg101*-mutant *Drosophila* adult wing sensory neurons (Lin et al., 2021). Thus, while ESCRT has many cellular activities, our experiments separate these functions to specifically narrow down its role in neuronal exosome release.

Our data also raise the possibility of a novel synaptic proteostasis mechanism which might be termed "endosomophagy", as has been seen in cell culture (Millarte et al., 2022; Wang et al., 2022; Zellner et al., 2021), and adds to the numerous intersections between endolysosomal traffic and autophagy in neurons (Boecker and Holzbaur, 2019). Many organelles are selectively targeted for macroautophagy via compartment-specific receptors (Lamark and Johansen, 2021), but such a process has not been specifically described for neuronal endosomes/MVEs. Our results suggest that autophagy is induced in ESCRT mutant synapses, presumably to dispose of aberrant endosomes, with different outcomes in Tsg101^{KD} versus *Hrs* mutants. Tsg101^{KD} led to aberrant autophagic vacuoles and reduced autophagic flux, perhaps due to a secondary role for ESCRT-1/Tsg101 in phagophore closure (Takahashi et al., 2019) or another step of autophagy. By contrast we found that *Hrs* mutants do not show these structures, either by light microscopy of the autophagic flux reporter GFP-mCherry-ATG8, or in previously published TEM of the NMJ (Lloyd et al., 2002). Instead, *Hrs* mutants exhibit induction of autophagy but normal autophagic flux in motor neurons, together with a moderate reduction in exosome cargo levels. Together, these results suggest that aberrant exosome-cargo-containing MVEs may be removed from *Hrs* mutant synapses by a compensatory, Tsg101-dependent autophagy pathway.

Implications for the physiological functions of exosomes

The majority of functional studies of EVs involve isolating EV subpopulations (at various degrees of homogeneity) from cell culture supernatants, applying them to target cells or tissues, and assessing their biological effects (Théry et al., 2018). Additional mechanistic insight has been obtained by eliminating specific cargo molecules from the donor cells before EV isolation, to determine if these molecules are required for EV bioactivity. While these approaches are very useful for determining therapeutic uses for EVs, they have several major limitations for understanding their normal functions *in vivo*. First, it is difficult to determine the concentration of EVs that a target cell would normally encounter, in order to design a physiologically relevant experiment. Second, while these types of experiments inform what EVs can do, they do not show that EV transfer is necessary for that signaling function *in vivo*. Removing the signaling cargo from the donor cell also does not show the necessity of EV transfer for biological functions, since the cargo could be acting cell autonomously in the donor cell, or could signal to a neighboring cell by another trafficking route. Indeed, previous studies at the *Drosophila* larval NMJ, which has been an important model system for the *in vivo* functions of EV traffic, have conducted tests for EV cargo activity in *evi* or *rab11* mutants, though we and others have shown that this results in depletion of cargo from the presynaptic donor cell in addition to loss of EVs (Ashley et al., 2018; Blanchette et al., 2022; Korkut et al., 2013, 2009; Walsh et al., 2021). Ultimately, determining if transfer of a cargo in EVs is necessary for its signaling function requires blocking EV transfer specifically, which we were able to achieve at ESCRT-depleted synapses.

Neuronally derived Wg is required and sufficient for synaptic growth, and is required together with glia-derived Wg to organize postsynaptic glutamate receptor fields (Kerr et al., 2014; Miech et al., 2008; Packard et al., 2002). Therefore, if transsynaptic transfer of Evi was required for Wg signaling, we would have expected to see a dramatic reduction in synaptic growth at ESCRT-depleted synapses, as well as disruptions in postsynaptic development and organization (Korkut et al., 2009; Miech et al., 2008; Packard et al., 2002). Instead, we observed no significant change in bouton or active zone number relative to controls. *wg*-phenocopying defects in postsynaptic development were also not observed by electron microscopy in CHMPIIB^{intron5} (West et al., 2015) or *Hrs*-mutant synapses (Lloyd et al., 2002), or in our data from ESCRT mutants. Similarly, Hsp90 mutants attenuate Evi exosome release by disrupting MVE-plasma membrane fusion, but do not result in a strong disruption of active zone or postsynaptic development (Lauwers et al., 2018). Thus, Evi release in exosomes does not correlate with effective Wg signaling. Importantly, it is likely that Hsp90 and ESCRT mutant synapses do secrete Wg, albeit by conventional secretion rather than an exosomal mechanism (Beckett et al., 2013), and that the primary function for Evi is to traffic Wg to the presynaptic terminal and maintain its levels there. However, we did find that knockdown of the ESCRT components Tsg101 and Shrub recapitulated one phenotype of *evi* and *Wg* mutants, which is an increase in developmentally arrested ghost boutons. This suggests that transynaptic transfer of Evi and Wg may be required for some aspects of assembly of the post-synaptic apparatus during larval development.

Syt4 protein is thought to act in the postsynaptic muscle (Adolfsen et al., 2004; Barber et al., 2009; Harris et al., 2016), but its endogenous transcript is not expressed in this tissue, leading to the prevailing model of transynaptic transfer from the presynaptic neuron in exosomes (Korkut et al., 2013). However, our results show that transynaptic

transfer in exosomes can be blocked without affecting the signaling activities of Syt4, and that the majority of postsynaptic Syt4 is not exposed to the muscle cytoplasm. The main evidence for a muscle requirement for Syt4 is that re-expression of Syt4 using muscle-specific GAL4 drivers is sufficient to rescue structural and functional plasticity defects of the *syt4* null mutant (Korkut et al., 2013; Piccioli and Littleton, 2014; Yoshihara et al., 2005). This is difficult to reconcile with our findings that Tsg101^{KD} animals lack detectable postsynaptic Syt4, but do not phenocopy *syt4* mutants. There are several possible explanations for this conundrum. First, we cannot completely rule out the possibility that small amounts of residual exosomal Syt4 after Tsg101 knockdown (perhaps transferred by a non-exosomal pathway, and distributed diffusely in the muscle) are sufficient to drive a transynaptic signal. An argument against this possibility is that *nwk* and *rab11* mutants also have trace amounts of Syt4 postsynaptically, and do strongly phenocopy the *syt4* null mutant (presumably since they also deplete Syt4 from the presynaptic compartment) (Korkut et al., 2013; Walsh et al., 2021; Blanchette et al., 2022). Second, it is possible that the muscle GAL4 drivers used in these previous rescue studies have some leaky expression in the neuron. Third, ectopically muscle-expressed Syt4 might have a neomorphic function in the muscle that bypasses the loss of neuronal Syt4, or else it could be retrogradely transported to the neuron. Indeed, muscle-expressed Syt4 is localized in close apposition to the presynaptic membrane (Harris et al., 2016).

Conclusion

Why are Evi and Syt4 trafficked into exosomes, if not for a signaling function? Local exosome release could serve as a proteostatic mechanism for synapse-specific control of signaling cargo levels. Indeed, the amount of cargo loaded into exosomes could be tuned by regulating endosomal sorting via retromer (Walsh et al., 2021), or by controlling the rate of endocytic flux into the Rab11-dependent recycling pathway (Blanchette et al., 2022). Through these mechanisms, neurons might achieve local control of synaptogenic or plasticity-inducing signaling pathways, in a much more rapid and spatially directed fashion than transcriptional or translational regulation. Importantly, our results do not rule out signaling functions for these cargoes in other contexts or neuronal cell types, or for other EV cargoes. Indeed, extensive evidence supports signaling functions for neuronal EVs in multiple contexts (Gassama and Favereaux, 2021; Lizarraga-Valderrama and Sheridan, 2021; Schnatz et al., 2021). However, our data encourage future hypothesis-challenging experiments for EV functions using membrane trafficking mutants that disrupt EV release specifically.

Materials and Methods

Drosophila culture

Flies were cultured using standard media and techniques. Flies used for experiments were maintained at 25°C, except for experiments using Shrub-RNAi, which were maintained at 20°C. For detailed information on fly stocks used, see **Table S1**, and for detailed genotype information for each figure panel, see **Table S3**.

Immunohistochemistry

Wandering 3rd instar larvae were dissected in HL3.1 and fixed in HL3.1 with 4% paraformaldehyde for 45 minutes. Washes and antibody dilutions were conducted using PBS containing 0.2% Triton X-100 (0.2% PBX). Primary antibody incubations were conducted overnight at 4°C, and secondary antibody incubations for 1-2 hours at room temperature. α-HRP incubations were conducted either overnight at 4°C or for 1-2 hours at room temperature. Prior to imaging, fillets were mounted on slides with Vectashield (Vector Labs). For detailed information on antibodies used in this study, see **Table S2**.

Activity-induced synaptic growth

High K^+ spaced stimulation was performed as described (Piccioli and Littleton, 2014). Briefly, 3rd instar larvae were dissected in HL3 solution at room temperature (in mM, 70 $NaCl_2$, 5 KCl, 0.2 $CaCl_2$, 20 $MgCl_2$, 10 $NaHCO_3$, 5 trehalose, 115 sucrose, and 5 HEPES (pH=7.2)). Dissecting pins were then moved inward to relax the fillet to 60% of its original size, and then stimulated 3 times in high K^+ solution (in mM, 40 $NaCl_2$, 90 KCl, 1.5 $CaCl_2$, 20 $MgCl_2$, 10 $NaHCO_3$, 5 trehalose, 5 sucrose, and 5 HEPES (pH=7.2)) for 2 minutes each, with 10-minute HL3 incubations in between stimulation while on a shaker at room temperature. Following the 3rd and final stimulation, larvae were incubated in HL3 (approximately 2 minutes) and stretched to their initial length. Mock stimulations were performed identically to the high K^+ stimulation assay, except HL3 solution was used in place of high K^+ solution. Larvae were then fixed in 4% PFA in HL3 solution for 15 minutes and then stained and mounted as above.

Electrophysiology

Wandering 3rd instar larvae were dissected in HL3 saline (Stewart et al., 1994). Recordings were taken using an AxoClamp 2B amplifier (Axon Instruments, Burlingame, CA). A recording electrode was filled with 3M KCl and inserted into muscle 6 at abdominal segments A3 or A4. A stimulating electrode filled with saline was used to stimulate the severed segmental nerve using an isolated pulse stimulator (2100; A-M Systems). HFMR was induced by four trains of 100 Hz stimuli spaced 2 s apart in 0.3 mM extracellular Ca^{2+}. Miniature excitatory junctional potentials (minis) were recorded 2 min before and 10 min after HFMR induction. Mini frequency at indicated time points was calculated in 10-s bins. Fold enhancement was calculated by normalizing to the baseline mini frequency recorded prior to HFMR induction. Analyses were performed using Clampfit 10.0 software (Molecular Devices, Sunnyvale, CA). Each n value represents a single muscle recording, with data generated from at least six individual larvae of each genotype arising from at least two independent crosses. Resting membrane potentials were between -50 mV and -75 mV and were not different between genotypes. Input resistances were between 5 MΩ and 10 MΩ and were not different between genotypes.

Electron microscopy

Wandering 3rd instar larvae were dissected and fixed in 1% glutaraldehyde and 4% paraformaldehyde in 1% (0.1M) sodium cacodylate buffer overnight at 4°C. Samples were postfixed in 1% osmium tetroxide and 1.5% potassium ferrocyanide for 1 h, then 1% aqueous uranyl acetate for 0.5 h. Stepwise dehydration was conducted for 10 min each in 30%, 50%, 70%, 85%, and 95% ethanol, followed by 2× 10 min in 100% ethanol. Samples were transferred to 100% propylene oxide for 1 h, then 3:1 propylene oxide and 812 TAAB Epon Resin (epon, TAAB Laboratories Equipment Ltd.) for 1 h, then 1:1 propylene oxide:epon for 1 h and then left overnight in a 1:3 mixture of propylene oxide:epon. Samples were then transferred to fresh epon for 2 h. Samples were then flat-embedded and polymerized at 60°C for 48 h, and remounted for sectioning. 70-µm-thin sections were cut on a Leica UC6 Ultramicrotome (Leica Microsystems), collected onto 2X1 mm slot grids coated with formvar and carbon, and then poststained with lead citrate (Venable and Coggeshall, 1965). Grids were imaged using a FEI Morgagni transmission electron microscope (FEI) operating at 80 kV and equipped with an AMT Nanosprint5 camera.

Imaging and quantification

Acquisition: Analysis of EV cargoes and bouton morphology were conducted at muscle 6/7 NMJ from segments A2 and A3, or for **Fig. 4A** at muscle 4 from segments A2-A4. Z-stacks were acquired using a Nikon Ni-E upright microscope equipped with a Yokogawa CSU-W1 spinning disk head, an Andor iXon 897U EMCCD camera, and Nikon Elements AR software. A 60X (n.a. 1.4) oil immersion objective was used to image NMJs, cell bodies, and fixed axons. Data in **Fig. S4C** were acquired with a Zeiss LSM 800 confocal microscope using a 40x (n.a. 1.4) oil immersion objective and Zen Black 2.3 software. For colocalization and puncta analysis branches from muscle 6/7 NMJ from segments A2 and A3 were taken using

Zen Blue software on a Zeiss LSM880 Fast Airyscan microscope in super resolution acquisition mode, using a 63X (n.a. 1.4) oil immersion objective. For axon transport, timelapse images were taken on the same Nikon Ni-E microscope described above. Images were taken of axon bundles proximal to the ventral ganglion (roughly within 100-300 µm). For APP transport, timelapse images were acquired for 3 minutes using 60X (n.a. 1.4) oil immersion objective. For mitochondria timelapse, images were acquired for 7 minutes using 60X (n.a. 1.0) water immersion objective. 9 Z slices were collected per frame (Step size 0.3 µm, with no acquisition delay between timepoints, resulting in a frame rate of 2.34-2.37 sec/frame). To visualize moving particles for mitochondria, a third of the axon in the field of view was photobleached using an Andor Mosaic digital micromirror device operated by Andor IQ software, to eliminate fluorescence from stationary particles that would interfere with visualization of particles moving into the bleached region. Image acquisition settings were identical for all images in each independent experiment.

EV quantification and colocalization: Volumetric analysis was performed using Volocity 6.0 software. For each image, both type 1s and 1b boutons were retained for analysis while axons were cropped out. The presynaptic volume was defined by an HRP threshold, excluding objects smaller than 7 μm^3 and closing holes. The postsynaptic region was defined by a 3 µm dilation of the HRP mask. However, for Evi-GFP, where the presynaptic signal vastly exceeded postsynaptic signal, we analyzed only the distal 2 µm of this postsynaptic dilation region to eliminate the bleed-over haze from the presynaptic signal. EV cargo and Rab signals were manually thresholded to select particles brighter than the muscle background. EV cargo integrated density in these thresholded puncta was normalized to the overall presynaptic volume. These values were further normalized to the mean of the control to produce a "normalized puncta intensity" value for each NMJ. For colocalization, the overlap of the two channels was measured in Volocity 6.0 and used for calculation of Mander's coefficients.

Quantification of electron micrographs: A single medial section of each bouton was selected for analysis. Two experimenters, blinded to genotype, together recorded the presence of autophagic vacuoles, including phagopores (double or dense membrane but not closed; note that depending on the plane of section, some of these may appear as autophagosomes), autophagosomes (contents with similar properties to the cytoplasm, fully enclosed in the section by a double membrane), and autolyososomes (contents are electron dense) (Lucocq and Hacker, 2013; Nagy et al., 2015). We also evaluated whether boutons lacked SSR, or featured postsynaptic pockets (electron-lucent areas extending at least 300 nm from the presynaptic membrane (Packard et al., 2002).

Quantification of GFP-mCherry-Atg8 distribution: A single field of view confocal stack (62x62 µm) from the larval ventral ganglion, containing 10-15 Vglut-expressing cell bodies, was manually thresholded in Volocity 6.0 software to segment and measure the volume and integrated fluorescence density of soma, GFP puncta, and mCherry puncta. The overlap between the GFP and mCherry channels was used for the calculation of the Mander's coefficient (fraction of total mCherry-puncta integrated density found in the GFP-puncta positive volume).

Axon and cell body measurements: To measure intensity of EV cargoes in axons, axons proximal to the ventral ganglion (within 100-300 µm) were imaged as described above. Images were analyzed in Fiji by making sum projections, cropping out unwanted debris or other tissue and making a mask on the HRP. The total intensity of the EV cargo was measured within the masked HRP area. For cell bodies, EV cargo intensity was measured from a middle slice through the motor neuron cell body layer of the ventral ganglion using Fiji.

Quantification of live axonal trafficking of APP-GFP and Mito-GFP puncta: To quantify APP-GFP and mitochondria dynamics in live axons, maximum intensity projections of time course images were processed in Fiji to subtract background and adjust for XY drift using the StackReg plugin. Kymographs were generated from 1-4 axons per animal using the Fiji plugin KymographBuilder. Kymographs were blinded and number of tracks were manually counted. The minimum track length measured was 3 µm with most tracks above 5 µm. Velocity was measured by calculating the slope of the identified tracks.

Bouton quantification: The experimenter was blinded to genotypes and then manually counted the total number of type 1 synaptic boutons on the NMJ on muscle 6 and 7 in the abdominal segments A2 and A3 of third instar wandering larvae. A synaptic bouton was considered each spherical varicosity, defined by the presence of the synaptic vesicle marker Synaptotagmin 1, the active zone marker Bruchpilot (Brp) and the neuronal membrane marker Hrp. For quantifying ghost boutons (basal and activity-induced), the experimenter was blinded to genotype and condition and ghost boutons were quantified as α-HRP-positive structures with a visible connection to the main NMJ arbor, and without α-DLG staining. For quantifying DLG "featheriness", the experimenter was blinded to genotype and scored the number of NMJs with at least one region of fenestrated Dlg that extended far from the bouton periphery.

Active zone quantification
To count the active zones in fluorescence micrographs, Brp-stained punctae were assessed on maximum intensity projection images. The Trainable Weka Segmentation (TWS) machine-learning tool (https://doi.org/10.1093/bioinformatics/btx180) in Fiji was used to manually annotate Brp-positive punctae with different fluorescence intensities, and to train a classifier that automatically segmented the Brp-positive active zones. The objects segmented via the applied classifier were subjected to Huang auto thresholding to obtain binary masks. Next, we applied a Watershed processing on the binary image, to improve the isolation of individual neighboring active zones from the diffraction limited images. We performed particle analysis on the segmented active zones and obtained their number, area, and integrated density. The number of active zones was normalized to the NMJ area. To determine the NMJ area using TWS, we trained the classifier by annotating the HRP positive NMJ on maximum intensity projections of the HRP channel. Axons were manually cropped from the image before TWS. The segmented HRP area was subjected to Huang auto thresholding, the binary masks were selected and the NMJ area was obtained via the "Analyze particle" function in FIJI of particles larger than 5 µm (to eliminate from the analysis residual HRP EV debris segmented in a very few images).

Statistics
All statistical measurements were performed in GraphPad Prism 6 (see **Table S3**). Comparisons were made separately for presynaptic and postsynaptic datasets, due to differences between these compartments for intensity, signal-to-noise ratio, and variance. Datasets were tested for normality, and statistical significance was tested using unpaired two-tailed Student's *t* tests or Mann–Whitney tests (if number of conditions was two) or ANOVA followed by Tukey's tests or Kruskal–Wallis followed by Dunn's test (if number of conditions was greater than two). For categorical measurements of autophagic vacuoles and DLG distribution, Fisher's exact test was used. Statistical significance is indicated as *P < 0.05; **P < 0.01; ***P < 0.001.

Acknowledgements
We thank the Developmental Studies Hybridoma Bank created by the NICHD of the NIH, and the Bloomington *Drosophila* Stock Center (Indiana University, Bloomington, IN, NIH P40OD018537). We thank Berith Isaac and the Brandeis Electron Microscopy Facility for assistance with EM, Michael Boutros, Josie Clowney, and Tor Erik Ruston for fly lines, Harald Stenmark for discussion of endosomophagy, and Cassie Blanchette and Steve Del Signore for comments on the manuscript. This work was supported by NINDS grants R01 NS103967 to A.A.R. and F32 NS120909 to E.C.D.

Author contributions
ECD, KPH, KK, MFP, BAS, AAR designed the study and experiments. ECD, KPH, KK, , MFP, MR, RCS conducted the experiments. ECD, KPH, KK, MFP, BE, MR, RCS and AAR performed the analyses. ECD and AAR wrote the manuscript, and all authors edited the manuscript. This article contains supporting information (4 Supplemental Figures and 3 tables).

Competing interest statement
The authors declare no competing financial interests.

References
Adolfsen B, Saraswati S, Yoshihara M, Littleton JT. 2004. Synaptotagmins are trafficked to distinct subcellular domains including the postsynaptic compartment. *J Cell Biol* **166**:249–260. doi:10.1083/jcb.200312054

Arbo BD, Cechinel LR, Palazzo RP, Siqueira IR. 2020. Endosomal dysfunction impacts extracellular vesicle release: Central role in Aβ pathology. *Ageing Res Rev* **58**:101006. doi:10.1016/j.arr.2019.101006

Asai H, Ikezu S, Tsunoda S, Medalla M, Luebke J, Haydar T, Wolozin B,

Butovsky O, Kügler S, Ikezu T. 2015. Depletion of microglia and inhibition of exosome synthesis halt tau propagation. *Nat Neurosci* **18**:1584–1593. doi:10.1038/nn.4132

Ashley J, Cordy B, Lucia D, Fradkin LG, Budnik V, Thomson T. 2018. Retrovirus-like Gag Protein Arc1 Binds RNA and Traffics across Synaptic Boutons. *Cell* **172**:262-274.e11. doi:10.1016/j.cell.2017.12.022

Ataman B, Ashley J, Gorczyca M, Ramachandran P, Fouquet W, Sigrist SJ, Budnik V. 2008. Rapid Activity-Dependent Modifications in Synaptic Structure and Function Require Bidirectional Wnt Signaling. *Neuron* **57**:705–718. doi:10.1016/j.neuron.2008.01.026

Barber CF, Jorquera RA, Melom JE, Littleton JT. 2009. Postsynaptic regulation of synaptic plasticity by synaptotagmin 4 requires both C2 domains. *J Cell Biol* **187**:295–310. doi:10.1083/jcb.200903098

Beckett K, Monier S, Palmer L, Alexandre C, Green H, Bonneil E, Raposo G, Thibault P, Le Borgne R, Vincent J-P. 2013. *Drosophila* S2 cells secrete wingless on exosome-like vesicles but the wingless gradient forms independently of exosomes. *Traffic* **14**:82–96. doi:10.1111/tra.12016

Birdsall V, Kirwan K, Zhu M, Imoto Y, Wilson SM, Watanabe S, Waites CL. 2022. Axonal transport of Hrs is activity dependent and facilitates synaptic vesicle protein degradation. *Life Sci Alliance* **5**:e202000745. doi:10.26508/lsa.202000745

Blanchette CR, Rodal AA. 2020. Mechanisms for biogenesis and release of neuronal extracellular vesicles. *Curr Opin Neurobiol* **63**:104–110. doi:10.1016/j.conb.2020.03.013

Blanchette CR, Scalera AL, Harris KP, Zhao Z, Dresselhaus EC, Koles K, Yeh A, Apiki JK, Stewart BA, Rodal AA. 2022a. Local regulation of extracellular vesicle traffic by the synaptic endocytic machinery. *J Cell Biol* **221**:e202112094. doi:10.1083/jcb.202112094

Boecker CA, Holzbaur ELF. 2019. Vesicular degradation pathways in neurons: at the crossroads of autophagy and endo-lysosomal degradation. *Curr Opin Neurobiol* **57**:94–101. doi:10.1016/j.conb.2019.01.005

Budnik V, Ruiz-Cañada C, Wendler F. 2016. Extracellular vesicles round off communication in the nervous system. *Nat Rev Neurosci* **17**:160–172. doi:10.1038/nrn.2015.29

Buratta S, Tancini B, Sagini K, Delo F, Chiaradia E, Urbanelli L, Emiliani C. 2020. Lysosomal Exocytosis, Exosome Release and Secretory Autophagy: The Autophagic- and Endo-Lysosomal Systems Go Extracellular. *Int J Mol Sci* **21**:2576. doi:10.3390/ijms21072576

Caussinus E, Kanca O, Affolter M. 2011. Fluorescent fusion protein knockout mediated by anti-GFP nanobody. *Nat Struct Mol Biol* **19**:117–121. doi:10.1038/nsmb.2180

Cone AS, Hurwitz SN, Lee GS, Yuan X, Zhou Y, Li Y, Meckes DG. 2020. Alix and Syntenin-1 direct amyloid precursor protein trafficking into extracellular vesicles. *BMC Mol Cell Biol* **21**:58. doi:10.1186/s12860-020-00302-0

Coulter ME, Dorobantu CM, Lodewijk GA, Delalande F, Cianferani S, Ganesh VS, Smith RS, Lim ET, Xu CS, Pang S, Wong ET, Lidov HGW, Calicchio ML, Yang E, Gonzalez DM, Schlaeger TM, Mochida GH, Hess H, Lee W-CA, Lehtinen MK, Kirchhausen T, Haussler D, Jacobs FMJ, Gaudin R, Walsh CA. 2018. The ESCRT-III Protein CHMP1A Mediates Secretion of Sonic Hedgehog on a Distinctive Subtype of Extracellular Vesicles. *Cell Rep* **24**:973-986.e8. doi:10.1016/j.celrep.2018.06.100

Das S, Yu S, Sakamori R, Stypulkowski E, Gao N. 2012. Wntless in Wnt secretion: molecular, cellular and genetic aspects. *Front Biol* **7**:587–593. doi:10.1007/s11515-012-1200-8

Dinkins MB, Enasko J, Hernandez C, Wang G, Kong J, Helwa I, Liu Y, Terry AV, Bieberich E. 2016. Neutral Sphingomyelinase-2 Deficiency Ameliorates Alzheimer's Disease Pathology and Improves Cognition in the 5XFAD Mouse. *J Neurosci* **36**:8653–8667. doi:10.1523/JNEUROSCI.1429-16.2016

Doyotte A, Russell MRG, Hopkins CR, Woodman PG. 2005. Depletion of TSG101 forms a mammalian `Class E' compartment: a multicisternal early endosome with multiple sorting defects. *J Cell Sci* **118**:3003–3017. doi:10.1242/jcs.02421

Dubey SK, Maulding K, Sung H, Lloyd TE. 2022. Nucleoporins are degraded via upregulation of ESCRT-III/Vps4 complex in *Drosophila* models of C9-ALS/FTD. *Cell Rep* **40**:111379. doi:10.1016/j.celrep.2022.111379

Fauré J, Lachenal G, Court M, Hirrlinger J, Chatellard-Causse C, Blot B, Grange J, Schoehn G, Goldberg Y, Boyer V, Kirchhoff F, Raposo G, Garin J, Sadoul R. 2006. Exosomes are released by cultured cortical neurones. *Mol Cell Neurosci* **31**:642–648. doi:10.1016/j.mcn.2005.12.003

Fernandes AR, Mendes CS, Gomes ER, Teodoro RO. 2021. Motor neuron boutons remodel through membrane blebbing. doi:10.1101/2021.03.07.434250

Filimonenko M, Stuffers S, Raiborg C, Yamamoto A, Malerød L, Fisher EMC, Isaacs A, Brech A, Stenmark H, Simonsen A. 2007. Functional multivesicular bodies are required for autophagic clearance of protein aggregates associated with neurodegenerative disease. *J Cell Biol* **179**:485–500. doi:10.1083/jcb.200702115

Fuentes-Medel Y, Logan MA, Ashley J, Ataman B, Budnik V, Freeman MR. 2009. Glia and muscle sculpt neuromuscular arbors by engulfing destabilized synaptic boutons and shed presynaptic debris. *PLoS Biol* **7**:e1000184. doi:10.1371/journal.pbio.1000184

Gassama Y, Favereaux A. 2021. Emerging Roles of Extracellular Vesicles in the Central Nervous System: Physiology, Pathology, and Therapeutic Perspectives. *Front Cell Neurosci* **15**:626043. doi:10.3389/fncel.2021.626043

Goncalves MB, Malmqvist T, Clarke E, Hubens CJ, Grist J, Hobbs C, Trigo D, Risling M, Angeria M, Damberg P, Carlstedt TP, Corcoran JPT. 2015. Neuronal RARβ Signaling Modulates PTEN Activity Directly in Neurons and via Exosome Transfer in Astrocytes to Prevent Glial Scar Formation and Induce Spinal Cord Regeneration. *J Neurosci* **35**:15731–15745. doi:10.1523/JNEUROSCI.1339-15.2015

Gong J, Körner R, Gaitanos L, Klein R. 2016. Exosomes mediate cell contact–independent ephrin-Eph signaling during axon guidance. *J Cell Biol* **214**:35–44. doi:10.1083/jcb.201601085

Gruenberg J. 2020. Life in the lumen: The multivesicular endosome. *Traffic* **21**:76–93. doi:10.1111/tra.12715

Guo BB, Bellingham SA, Hill AF. 2015. The neutral sphingomyelinase pathway regulates packaging of the prion protein into exosomes. *J Biol Chem* **290**:3455–3467. doi:10.1074/jbc.M114.605253

Harris KP, Zhang YV, Piccioli ZD, Perrimon N, Littleton JT. 2016. The postsynaptic t-SNARE Syntaxin 4 controls traffic of Neuroligin 1 and Synaptotagmin 4 to regulate retrograde signaling. *eLife* **5**:e13881. doi:10.7554/eLife.13881

Holm MM, Kaiser J, Schwab ME. 2018. Extracellular Vesicles: Multimodal Envoys in Neural Maintenance and Repair. *Trends Neurosci* **41**:360–372. doi:10.1016/j.tins.2018.03.006

Kerr KS, Fuentes-Medel Y, Brewer C, Barria R, Ashley J, Abruzzi KC, Sheehan A, Tasdemir-Yilmaz OE, Freeman MR, Budnik V. 2014. Glial wingless/Wnt regulates glutamate receptor clustering and synaptic physiology at the *Drosophila* neuromuscular junction. *J Neurosci* **34**:2910–2920. doi:10.1523/JNEUROSCI.3714-13.2014

Klionsky DJ, et al. 2021. Guidelines for the use and interpretation of assays for monitoring autophagy (4th edition)1. *Autophagy* **17**:1–382. doi:10.1080/15548627.2020.1797280

Koles K, Nunnari J, Korkut C, Barria R, Brewer C, Li Y, Leszyk J, Zhang B, Budnik V. 2012. Mechanism of evenness interrupted (Evi)-exosome release at synaptic boutons. *J Biol Chem* **287**:16820–16834. doi:10.1074/jbc.M112.342667

Koles K, Yeh AR, Rodal AA. 2015. Tissue-specific tagging of endogenous loci in *Drosophila melanogaster*. *Biol Open* **5**:83–89. doi:10.1242/bio.016089

Korkut C, Ataman B, Ramachandran P, Ashley J, Barria R, Gherbesi N, Budnik V. 2009. Trans-synaptic transmission of vesicular Wnt signals through Evi/Wntless. *Cell* **139**:393–404. doi:10.1016/j.cell.2009.07.051

Korkut C, Li Y, Koles K, Brewer C, Ashley J, Yoshihara M, Budnik V. 2013. Regulation of postsynaptic retrograde signaling by presynaptic exosome release. *Neuron* **77**:1039–1046. doi:10.1016/j.neuron.2013.01.013

Lachenal G, Pernet-Gallay K, Chivet M, Hemming FJ, Belly A, Bodon G, Blot B, Haase G, Goldberg Y, Sadoul R. 2011. Release of exosomes from differentiated neurons and its regulation by synaptic glutamatergic activity. *Mol Cell Neurosci* **46**:409–418. doi:10.1016/j.mcn.2010.11.004

Lamark T, Johansen T. 2021. Mechanisms of Selective Autophagy. *Annu Rev Cell Dev Biol* **37**:143–169. doi:10.1146/annurev-cellbio-120219-035530

Lauwers E, Wang Y-C, Gallardo R, Van der Kant R, Michiels E, Swerts J, Baatsen P, Zaiter SS, McAlpine SR, Gounko NV, Rousseau F, Schymkowitz J, Verstreken P. 2018. Hsp90 Mediates Membrane Deformation and Exosome Release. *Mol Cell* **71**:689-702.e9. doi:10.1016/j.molcel.2018.07.016

Lee SH, Shin SM, Zhong P, Kim H-T, Kim D-I, Kim JM, Heo WD, Kim D-W, Yeo C-Y, Kim C-H, Liu Q-S. 2018. Reciprocal control of excitatory synapse numbers by Wnt and Wnt inhibitor PRR7 secreted on exosomes. *Nat Commun* **9**:3434. doi:10.1038/s41467-018-05858-2

Lefebvre C, Legouis R, Culetto E. 2018. ESCRT and autophagies: Endosomal functions and beyond. *Semin Cell Dev Biol*, The multiple facets of the ESCRT machinery **74**:21–28. doi:10.1016/j.semcdb.2017.08.014

Leidal AM, Debnath J. 2021. Emerging roles for the autophagy machinery

in extracellular vesicle biogenesis and secretion. *FASEB BioAdvances* **3**:377–386. doi:10.1096/fba.2020-00138

Lin T-H, Bis-Brewer DM, Sheehan AE, Townsend LN, Maddison DC, Züchner S, Smith GA, Freeman MR. 2021. TSG101 negatively regulates mitochondrial biogenesis in axons. *Proc Natl Acad Sci U S A* **118**:e2018770118. doi:10.1073/pnas.2018770118

Lizarraga-Valderrama LR, Sheridan GK. 2021. Extracellular vesicles and intercellular communication in the central nervous system. *FEBS Lett* **595**:1391–1410. doi:10.1002/1873-3468.14074

Lloyd TE, Atkinson R, Wu MN, Zhou Y, Pennetta G, Bellen HJ. 2002. Hrs Regulates Endosome Membrane Invagination and Tyrosine Kinase Receptor Signaling in *Drosophila*. *Cell* **108**:261–269. doi:10.1016/S0092-8674(02)00611-6

Lucocq JM, Hacker C. 2013. Cutting a fine figure. *Autophagy* **9**:1443–1448. doi:10.4161/auto.25570

Men Y, Yelick J, Jin S, Tian Y, Chiang MSR, Higashimori H, Brown E, Jarvis R, Yang Y. 2019. Exosome reporter mice reveal the involvement of exosomes in mediating neuron to astroglia communication in the CNS. *Nat Commun* **10**:4136. doi:10.1038/s41467-019-11534-w

Miech C, Pauer H-U, He X, Schwarz TL. 2008. Presynaptic local signaling by a canonical wingless pathway regulates development of the *Drosophila* neuromuscular junction. *J Neurosci* **28**:10875–10884. doi:10.1523/JNEUROSCI.0164-08.2008

Millarte V, Schlienger S, Kälin S, Spiess M. 2022. Rabaptin5 targets autophagy to damaged endosomes and Salmonella vacuoles via FIP200 and ATG16L1. *EMBO Rep* **23**:e53429. doi:10.15252/embr.202153429

Moreau K, Renna M, Rubinsztein DC. 2013. Connections between SNAREs and autophagy. *Trends Biochem Sci* **38**:57–63. doi:10.1016/j.tibs.2012.11.004

Nagy P, Varga Á, Kovács AL, Takáts S, Juhász G. 2015. How and why to study autophagy in Drosophila: it's more than just a garbage chute. *Methods* **75**:151–161. doi:10.1016/j.ymeth.2014.11.016

Nakatogawa H. 2020. Mechanisms governing autophagosome biogenesis. *Nat Rev Mol Cell Biol* **21**:439–458. doi:10.1038/s41580-020-0241-0

O'Brien K, Ughetto S, Mahjoum S, Nair AV, Breakefield XO. 2022. Uptake, functionality, and re-release of extracellular vesicle-encapsulated cargo. *Cell Rep* **39**:110651. doi:10.1016/j.celrep.2022.110651

Packard M, Koo ES, Gorczyca M, Sharpe J, Cumberledge S, Budnik V. 2002. The Drosophila Wnt, wingless, provides an essential signal for pre- and postsynaptic differentiation. *Cell* **111**:319–330. doi:10.1016/s0092-8674(02)01047-4

Piccioli ZD, Littleton JT. 2014. Retrograde BMP Signaling Modulates Rapid Activity-Dependent Synaptic Growth via Presynaptic LIM Kinase Regulation of Cofilin. *J Neurosci* **34**:4371–4381. doi:10.1523/JNEUROSCI.4943-13.2014

Raymond CK, Howald-Stevenson I, Vater CA, Stevens TH. 1992. Morphological classification of the yeast vacuolar protein sorting mutants: evidence for a prevacuolar compartment in class E vps mutants. *Mol Biol Cell* **3**:1389–1402. doi:10.1091/mbc.3.12.1389

Rodahl LM, Haglund K, Sem-Jacobsen C, Wendler F, Vincent J-P, Lindmo K, Rusten TE, Stenmark H. 2009. Disruption of Vps4 and JNK Function in Drosophila Causes Tumour Growth. *PLoS ONE* **4**:e4354. doi:10.1371/journal.pone.0004354

Rusten TE, Vaccari T, Lindmo K, Rodahl LMW, Nezis IP, Sem-Jacobsen C, Wendler F, Vincent J-P, Brech A, Bilder D, Stenmark H. 2007. ESCRTs and Fab1 Regulate Distinct Steps of Autophagy. *Curr Biol* **17**:1817–1825. doi:10.1016/j.cub.2007.09.032

Sackmann V, Sinha MS, Sackmann C, Civitelli L, Bergström J, Ansell-Schultz A, Hallbeck M. 2019. Inhibition of nSMase2 Reduces the Transfer of Oligomeric α-Synuclein Irrespective of Hypoxia. *Front Mol Neurosci* **12**:200. doi:10.3389/fnmol.2019.00200

Schnatz A, Müller C, Brahmer A, Krämer-Albers E-M. 2021. Extracellular Vesicles in neural cell interaction and CNS homeostasis. *FASEB BioAdvances* **3**:577–592. doi:10.1096/fba.2021-00035

Sheehan P, Zhu M, Beskow A, Vollmer C, Waites CL. 2016. Activity-Dependent Degradation of Synaptic Vesicle Proteins Requires Rab35 and the ESCRT Pathway. *J Neurosci* **36**:8668–8686. doi:10.1523/JNEUROSCI.0725-16.2016

Sidibe DK, Vogel MC, Maday S. 2022. Organization of the autophagy pathway in neurons. *Curr Opin Neurobiol* **75**:102554. doi:10.1016/j.conb.2022.102554

Song Z, Xu Y, Deng W, Zhang L, Zhu H, Yu P, Qu Y, Zhao W, Han Y, Qin C. 2020. Brain Derived Exosomes Are a Double-Edged Sword in Alzheimer's Disease. *Front Mol Neurosci* **13**:79. doi:10.3389/fnmol.2020.00079

Soukup S-F, Kuenen S, Vanhauwaert R, Manetsberger J, Hernández-Díaz S, Swerts J, Schoovaerts N, Vilain S, Gounko NV, Vints K, Geens A, De Strooper B, Verstreken P. 2016. A LRRK2-Dependent EndophilinA Phosphoswitch Is Critical for Macroautophagy at Presynaptic Terminals. *Neuron* **92**:829–844. doi:10.1016/j.neuron.2016.09.037

Stewart BA, Atwood HL, Renger JJ, Wang J, Wu CF. 1994. Improved stability of Drosophila larval neuromuscular preparations in haemolymph-like physiological solutions. *J Comp Physiol [A]* **175**:179–191. doi:10.1007/BF00215114

Sweeney NT, Brenman JE, Jan YN, Gao F-B. 2006. The coiled-coil protein shrub controls neuronal morphogenesis in *Drosophila*. *Curr Biol CB* **16**:1006–1011. doi:10.1016/j.cub.2006.03.067

Takahashi Y, Liang X, Hattori T, Tang Z, He H, Chen H, Liu X, Abraham T, Imamura-Kawasawa Y, Buchkovich NJ, Young MM, Wang H-G. 2019. VPS37A directs ESCRT recruitment for phagophore closure. *J Cell Biol* **218**:3336–3354. doi:10.1083/jcb.201902170

Théry C, et al. 2018. Minimal information for studies of extracellular vesicles 2018 (MISEV2018): a position statement of the International Society for Extracellular Vesicles and update of the MISEV2014 guidelines. *J Extracell Vesicles* **7**:1535750. doi:10.1080/20013078.2018.1535750

Ugbode C, West RJH. 2021. Lessons learned from CHMP2B, implications for frontotemporal dementia and amyotrophic lateral sclerosis. *Neurobiol Dis* **147**:105144. doi:10.1016/j.nbd.2020.105144

van Niel G, D'Angelo G, Raposo G. 2018. Shedding light on the cell biology of extracellular vesicles. *Nat Rev Mol Cell Biol* **19**:213–228. doi:10.1038/nrm.2017.125

Venable JH, Coggeshall R. 1965. A SIMPLIFIED LEAD CITRATE STAIN FOR USE IN ELECTRON MICROSCOPY. *J Cell Biol* **25**:407–408. doi:10.1083/jcb.25.2.407

Vietri M, Radulovic M, Stenmark H. 2020. The many functions of ESCRTs. *Nat Rev Mol Cell Biol* **21**:25–42. doi:10.1038/s41580-019-0177-4

Vilcaes AA, Chanaday NL, Kavalali ET. 2021. Interneuronal exchange and functional integration of synaptobrevin via extracellular vesicles. *Neuron* **109**:971-983.e5. doi:10.1016/j.neuron.2021.01.007

Walsh RB, Dresselhaus EC, Becalska AN, Zunitch MJ, Blanchette CR, Scalera AL, Lemos T, Lee SM, Apiki J, Wang S, Isaac B, Yeh A, Koles K, Rodal AA. 2021. Opposing functions for retromer and Rab11 in extracellular vesicle traffic at presynaptic terminals. *J Cell Biol* **220**:e202012034. doi:10.1083/jcb.202012034

Wang BB, Xu H, Isenmann S, Huang C, Elorza-Vidal X, Rychkov GY, Estévez R, Schittenhelm RB, Lukacs GL, Apaja PM. 2022. Ubr1-induced selective endophagy/autophagy protects against the endosomal and Ca2+-induced proteostasis disease stress. *Cell Mol Life Sci CMLS* **79**:167. doi:10.1007/s00018-022-04191-8

Wang J, Fang N, Xiong J, Du Y, Cao Y, Ji W-K. 2021. An ESCRT-dependent step in fatty acid transfer from lipid droplets to mitochondria through VPS13D-TSG101 interactions. *Nat Commun* **12**:1252. doi:10.1038/s41467-021-21525-5

Wenzel EM, Schultz SW, Schink KO, Pedersen NM, Nähse V, Carlson A, Brech A, Stenmark H, Raiborg C. 2018. Concerted ESCRT and clathrin recruitment waves define the timing and morphology of intraluminal vesicle formation. *Nat Commun* **9**:2932. doi:10.1038/s41467-018-05345-8

West RJH, Lu Y, Marie B, Gao F-B, Sweeney ST. 2015. Rab8, POSH, and TAK1 regulate synaptic growth in a *Drosophila* model of frontotemporal dementia. *J Cell Biol* **208**:931–947. doi:10.1083/jcb.201404066

Willén K, Edgar JR, Hasegawa T, Tanaka N, Futter CE, Gouras GK. 2017. Aβ accumulation causes MVB enlargement and is modelled by dominant negative VPS4A. *Mol Neurodegener* **12**:61. doi:10.1186/s13024-017-0203-y

Yan M, Zheng T. 2021. Role of the endolysosomal pathway and exosome release in tau propagation. *Neurochem Int* **145**:104988. doi:10.1016/j.neuint.2021.104988

Yoshihara M, Adolfsen B, Galle KT, Littleton JT. 2005. Retrograde Signaling by Syt 4 Induces Presynaptic Release and Synapse-Specific Growth. *Science* **310**:858–863. doi:10.1126/science.1117541

Zellner S, Schifferer M, Behrends C. 2021. Systematically defining selective autophagy receptor-specific cargo using autophagosome content profiling. *Mol Cell* **81**:1337-1354.e8. doi:10.1016/j.molcel.2021.01.009

Zhen Y, Stenmark H. 2023. Autophagosome Biogenesis. *Cells* **12**:668. doi:10.3390/cells12040668

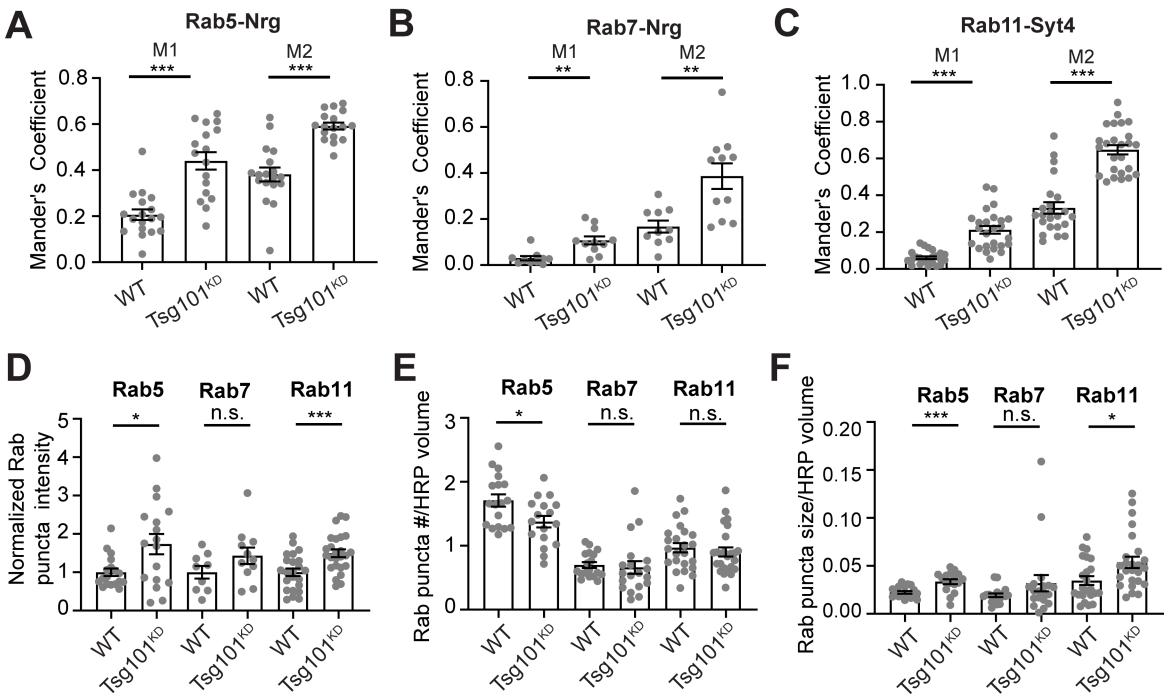

Figure S1: Synaptic EV cargoes accumulate in abnormal endosomal and autophagic structures upon neuronal Tsg101 knockdown (associated with Figure 2). **(A-C)** Quantification of co-localization of Nrg or Syt4 and Rab-GTPases upon neuronal Tsg101^{KD} (see Fig. 2A). Mander's coefficient for the colocalization of Nrg and Rab5 **(A)**, Nrg and Rab7 **(B)**, Syt4 and Rab11 **(C)**, where M1 indicates the fraction of EV cargo in the Rab-positive thresholded area and M2 is the fraction of the Rab marker in the EV cargo-positive thresholded area. **(D-F)** Quantification of Rab compartment properties: **(D)** normalized Rab puncta intensity, **(E)** density of Rab puncta in the presynaptic compartment, and **(F)** average size of Rab puncta.

Data is represented as mean +/- s.e.m.; n represents NMJs. All values except E and F are normalized to their respective controls. *p<0.05, **p<0.01, ***p<0.001. **See Tables S1 and S3 for detailed genotypes and statistical analyses.**

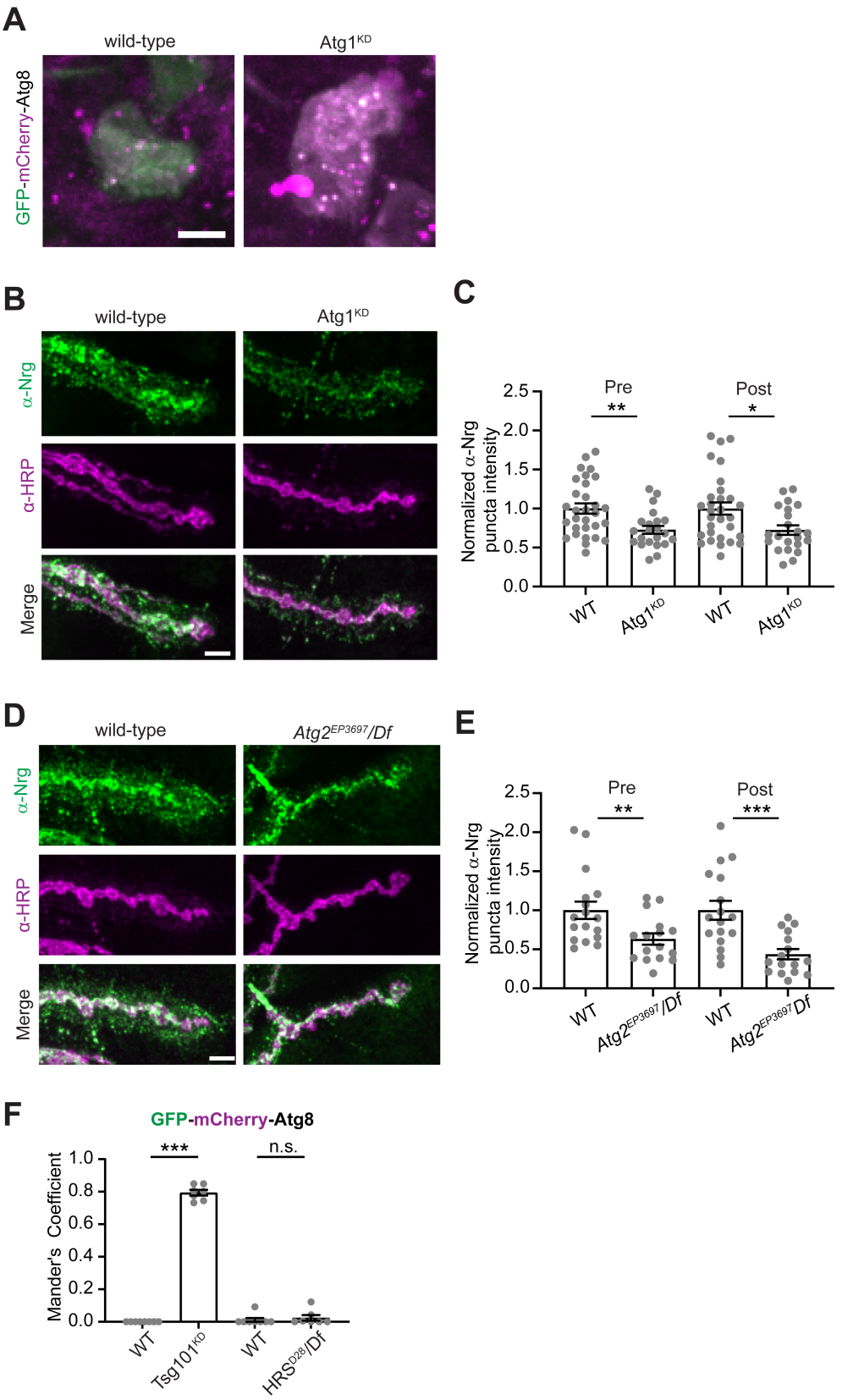

Figure S2. Autophagy is not strongly required for the release of EV cargoes (associated with Figure 2). **(A)** Representative confocal images of motor neuron cell bodies to validate that pan-neuronal Atg1 RNAi effectively blocks autophagic flux assessed by GFP-mCherry-Atg8. **(B)** Representative images of Nrg following motor neuron knockdown of *Atg1*. **(C)** Quantification of Nrg intensity from (B). **(D)** Representative confocal images of Nrg in wild-type versus *Atg2* null mutation. **(E)** Quantification of Nrg intensity from (D). **(F)** Colocalization of GFP and mCherry in cell bodies from motor neurons expressing GFP-mCherry-Atg8 (see Fig 2C).
All scale bars = 5 μm. Data is represented as mean +/- s.e.m.; n represents NMJs. *p<0.05, **p<0.01, ***p<0.001. **See Tables S1 and S3 for detailed genotypes and statistical analyses.**

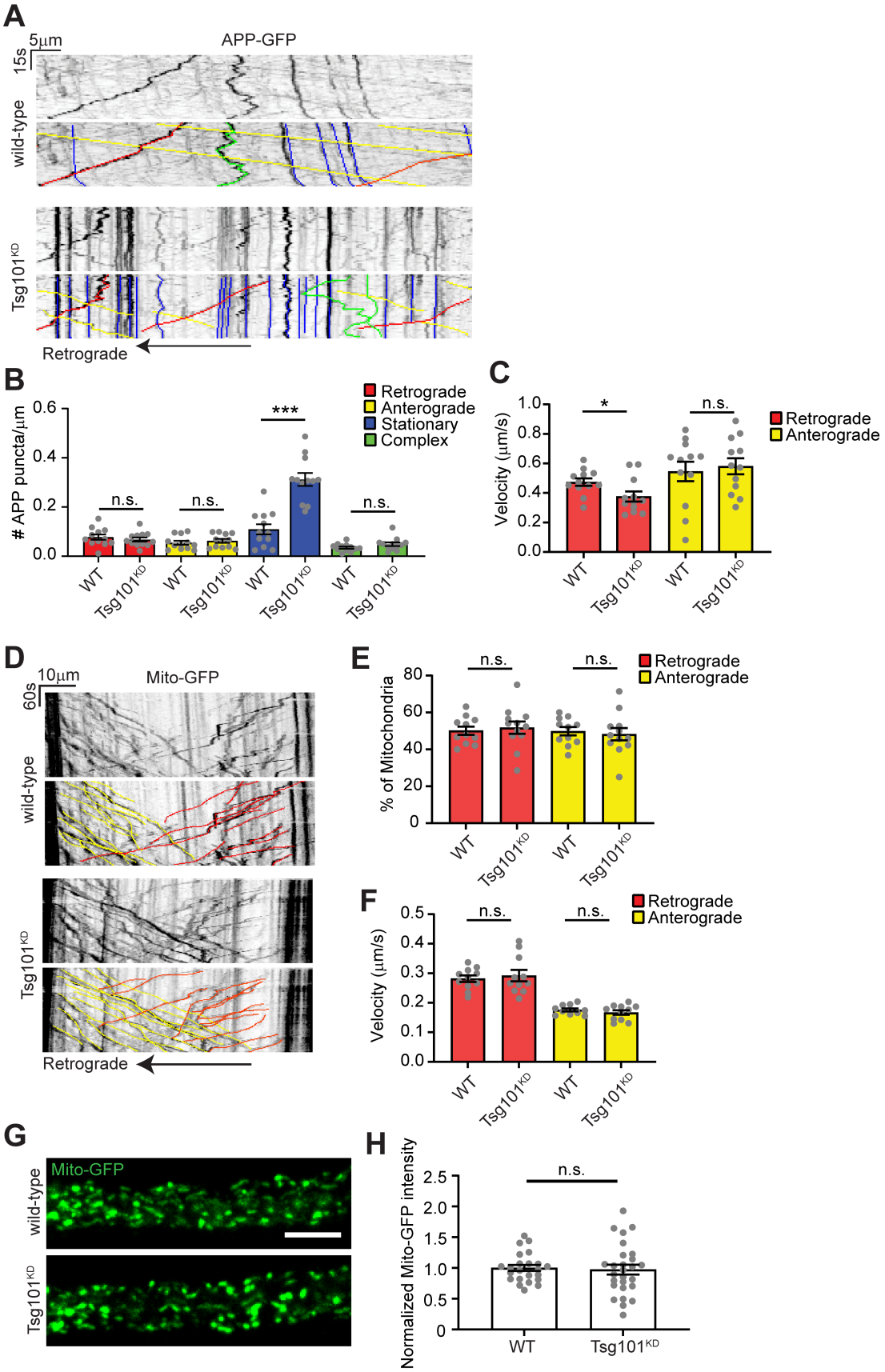

Figure S3. Axonal transport in Tsg101^{KD} larvae (associated with Figure 2). **(A)** Representative kymographs showing tracks of APP-GFP in the axon proximal to the ventral ganglion. Bottom panels show color coded traces. **(B)** Quantification of directionality of APP-GFP tracks. **(C)** Quantification of the velocity of retrograde and anterograde APP-GFP tracks upon neuronal Tsg101^{KD} (N represents animals). **(D)** Representative kymographs showing tracks of Mito-GFP in axonal region proximal to the ventral ganglion, following photobleaching. Lower panels show color coded traces. **(E)** Percent of mitochondria tracks moving retrograde and anterograde. (N represents axons). **(F)** Velocities of mitochondria tracks. **(G)** Representative images of the first frame of Mito-GFP videos. Scale bar = 10 μm. **(H)** Quantification of Mito-GFP puncta intensity from E.
Data is represented as mean +/- s.e.m. All values are normalized to their respective controls. *p<0.05, ***p<0.001. **See Tables S1 and S3 for detailed genotypes and statistical analyses.**

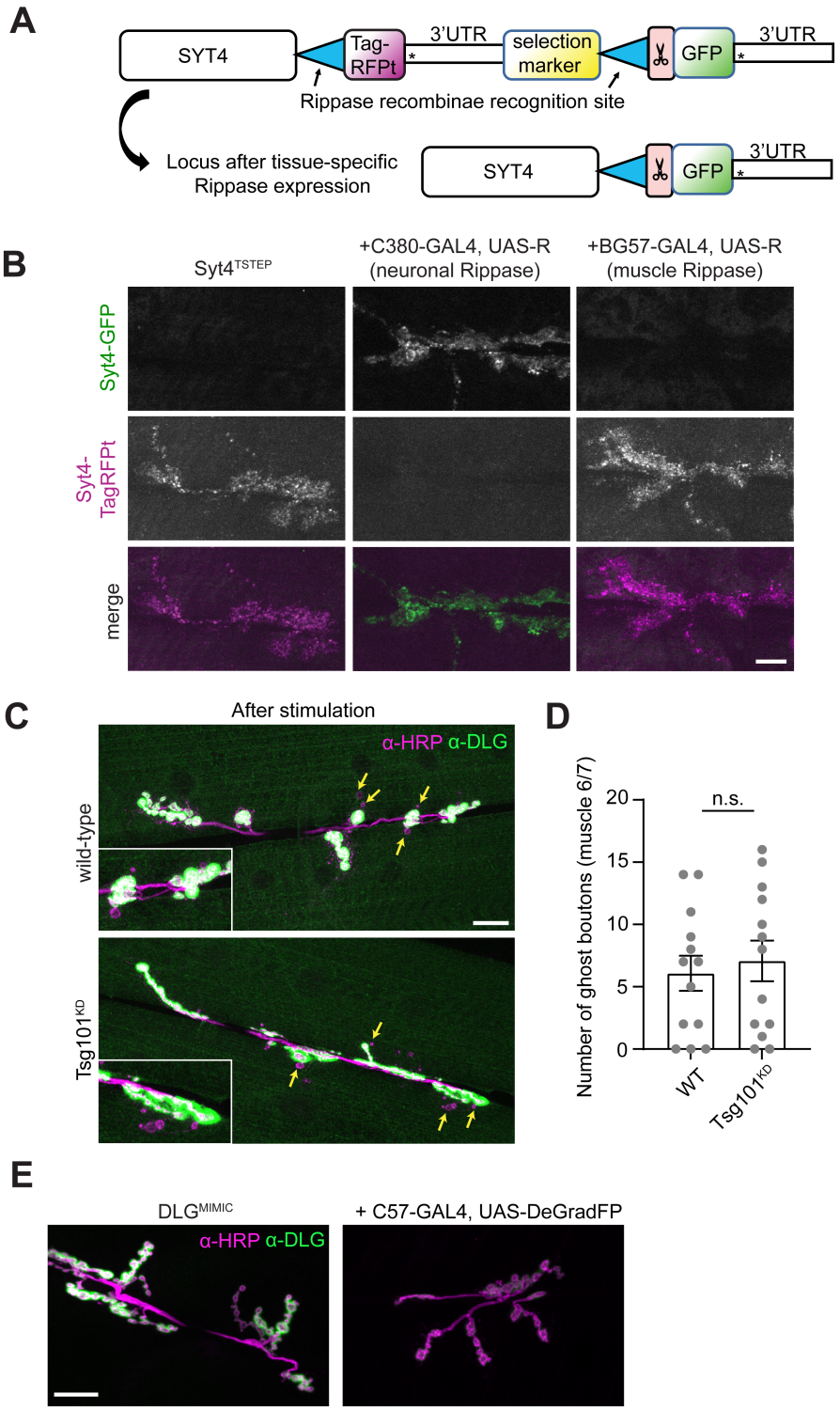

Figure S4. Tsg101^{KD} does not phenocopy *syt4* structural plasticity defects and is expressed only in the presynaptic neuron (associated with Figure 4). **(A-B)** Syt4 protein is derived from the presynaptic neuron. **(A)** Schematic for Tissue-Specific Tagging of Endogenous Proteins (T-STEP). Scissors indicate a Prescission protease cleavage site and * indicates stop codons. **(B)** Representative confocal images from muscle 6/7, showing Syt4^{TSTEP} expressed from its endogenous promoter, and switched from TagRFPt to GFP using either presynaptically (neuronal, C380-GAL4) or postsynaptically (muscle, C57-Gal4)-expressed recombinase (Rippase). Scale bar = 10 μm. **(C)** Representative confocal images from muscle 6/7 in spaced K^+-stimulated larvae. Arrows indicate ghost boutons. Scale bar = 20 μm. **(C)** Quantification of ghost bouton numbers per NMJ. Scale bar = 10 μm. **(E)** Representative images of Dlg^{MiMIC} (a postsynaptically-localized GFP knock-in) with muscle-expressed DeGradFP. Scale bar = 20 μm. Data is represented as mean +/- s.e.m.; n represents NMJs. **See Tables S1 and S3 for detailed genotypes and statistical analyses.**

Table S1: Fly Strains

Chromosome for transgene insertion indicated in roman numerals.

Experimental Models: Organism/allele		
GAL4^{C380} *(X)*	(Budnik et al., 1996)	Flybase ID: FBti0016294
GAL4^{Vglut} *(X)*	(Daniels et al., 2008)	Flybase ID: FBti0129146
GAL4^{C57} (III)	(Budnik et al., 1996)	Flybase ID: FBti0016293
w^{1118}	(Hazelrigg et al., 1984)	Flybase ID: FBal0018186
Syt4$^{EGFP\text{-}KI}$	(Walsh et al., 2021)	Flybase ID: FBal0368282
UAS-Evi-EGFP (II)	(Bartscherer et al., 2006)	Flybase ID: FBal0194740
UAS-APP-EGFP (II)	(Walsh et al., 2021)	Flybase ID: FBal0368284
GFP-Rab5-KI (II)	(Fabrowski et al., 2013)	Flybase ID: FBal0288693
YFP-myc-Rab7-KI (III)	(Dunst et al., 2015)	Flybase ID: FBal0314198
UAS-Mito-HA-GFP (II)		Flybase ID: FBst0008442
UAS-GFP-mCherry-Atg8 (II)		Flybase ID: FBst0037749
UAS-mCherry-RNAi (III)	(Perkins et al., 2015)	Flybase ID: FBal0260847
UAS-Luciferase-RNAi (III)	(Perkins et al., 2015)	Flybase ID: FBst0035788
UAS-Tsg101-RNAi^{GLV21075} (III) (Tsg101^{KD})	(Perkins et al., 2015)	Flybase ID: FBst0035710
UAS-Shrub-RNAi^{HMS01767} (II) (Shrub^{KD})	(Perkins et al., 2015)	Flybase ID: FBst0038305
UAS-Vps4^{DN} (II)	(Rodahl et al., 2009)	Flybase ID: FBtp0041057
Hrs^{D28}	(Lloyd et al., 2002)	Flybase ID: FBst0054574
Evi^{2}	(Bartscherer et al., 2006)	Flybase ID: FBal0194741
Df(2L)Exel6277 (removes Hrs)		Flybase ID: FBst0007744
UAS-Atg1-RNAi^{GL00047} (III) (Atg1^{KD})	(Perkins et al., 2015)	Flybase ID: FBst0035177
Atg2^{EP3697}	(Shen and Ganetzky, 2009)	Flybase ID: FBst0017156
Df(3L)Exel6091 (removes *Atg2*)		Flybase ID: FBst0007570
UAS-DegradGFP (II) (nSLimb-vhhGFP4)	(Urban et al., 2014)	Flybase ID: FBal0299649
Dlg1-MiMIC (X)	(Nagarkar-Jaiswal et al., 2015)	Flybase ID: FBst0059417

UAS-Rippase (III)	(Nern et al., 2011)	Flybase ID: FBst0055795
Syt4^{TSTEP}	(Walsh et al., 2021)	Flybase ID: FBti0216043

Table S2: Antibodies

REAGENT	SOURCE	IDENTIFIER	Concentration
Antibodies			
α-HRP-647	Jackson ImmunoResearch		1:250-1:500
α-Rab11	BD Biosciences	BD 610657	1:100
α-Dlg (mouse)	(Parnas et al., 2001), DSHB	4F3	1:500
α-Dlg (rabbit)	(Koh et al., 1999)		1:10000
α-Nrg	(Hortsch et al., 1990), DSHB	BP104	1:100
α-BRP	(Wagh et al., 2006), DSHB	nc82	1:100

Bartscherer K, Pelte N, Ingelfinger D, Boutros M. 2006. Secretion of Wnt ligands requires Evi, a conserved transmembrane protein. *Cell* **125**:523–533. doi:10.1016/j.cell.2006.04.009

Brook WJ, Cohen SM. 1996. Antagonistic interactions between wingless and decapentaplegic responsible for dorsal-ventral pattern in the *Drosophila* Leg. *Science* **273**:1373–1377. doi:10.1126/science.273.5280.1373

Budnik V, Koh YH, Guan B, Hartmann B, Hough C, Woods D, Gorczyca M. 1996. Regulation of synapse structure and function by the *Drosophila* tumor suppressor gene dlg. *Neuron* **17**:627–640. doi:10.1016/s0896-6273(00)80196-8

Daniels RW, Gelfand MV, Collins CA, DiAntonio A. 2008. Visualizing glutamatergic cell bodies and synapses in *Drosophila* larval and adult CNS. *J Comp Neurol* **508**:131–152. doi:10.1002/cne.21670

Dunst S, Kazimiers T, von Zadow F, Jambor H, Sagner A, Brankatschk B, Mahmoud A, Spannl S, Tomancak P, Eaton S, Brankatschk M. 2015. Endogenously Tagged Rab Proteins: A Resource to Study Membrane Trafficking in *Drosophila*. *Developmental Cell* **33**:351–365. doi:10.1016/j.devcel.2015.03.022

Fabrowski P, Necakov AS, Mumbauer S, Loeser E, Reversi A, Streichan S, Briggs JAG, De Renzis S. 2013. Tubular endocytosis drives remodelling of the apical surface during epithelial morphogenesis in *Drosophila*. *Nat Commun* **4**:2244. doi:10.1038/ncomms3244

Hazelrigg T, Levis R, Rubin GM. 1984. Transformation of white locus DNA in drosophila: dosage compensation, zeste interaction, and position effects. *Cell* **36**:469–481. doi:10.1016/0092-8674(84)90240-x

Hortsch M, Bieber AJ, Patel NH, Goodman CS. 1990. Differential splicing generates a nervous system-specific form of *Drosophila* neuroglian. *Neuron* **4**:697–709. doi:10.1016/0896-6273(90)90196-m

Koh YH, Popova E, Thomas U, Griffith LC, Budnik V. 1999. Regulation of DLG localization at synapses by CaMKII-dependent phosphorylation. *Cell* **98**:353–363. doi:10.1016/s0092-8674(00)81964-9

Lloyd TE, Atkinson R, Wu MN, Zhou Y, Pennetta G, Bellen HJ. 2002. Hrs Regulates Endosome Membrane Invagination and Tyrosine Kinase Receptor Signaling in *Drosophila*. *Cell* **108**:261–269. doi:10.1016/S0092-8674(02)00611-6

Marrus SB, Portman SL, Allen MJ, Moffat KG, DiAntonio A. 2004. Differential localization of glutamate receptor subunits at the *Drosophila* neuromuscular junction. *J Neurosci* **24**:1406–1415. doi:10.1523/JNEUROSCI.1575-03.2004

Nagarkar-Jaiswal S, Lee P-T, Campbell ME, Chen K, Anguiano-Zarate S, Gutierrez MC, Busby T, Lin W-W, He Y, Schulze KL, Booth BW, Evans-Holm M, Venken KJT, Levis RW, Spradling AC, Hoskins RA, Bellen HJ. 2015. A library of MiMICs allows tagging of genes and reversible, spatial and temporal knockdown of proteins in *Drosophila*. *Elife* **4**:e05338. doi:10.7554/eLife.05338

Nern A, Pfeiffer BD, Svoboda K, Rubin GM. 2011. Multiple new site-specific recombinases for use in manipulating animal genomes. *Proc Natl Acad Sci U S A* **108**:14198–14203. doi:10.1073/pnas.1111704108

Parnas D, Haghighi AP, Fetter RD, Kim SW, Goodman CS. 2001. Regulation of postsynaptic structure and protein localization by the Rho-type guanine nucleotide exchange factor dPix. *Neuron* **32**:415–424. doi:10.1016/s0896-6273(01)00485-8

Perkins LA, Holderbaum L, Tao R, Hu Y, Sopko R, McCall K, Yang-Zhou D, Flockhart I, Binari R, Shim H-S, Miller A, Housden A, Foos M, Randkelv S, Kelley C, Namgyal P, Villalta C, Liu L-P, Jiang X, Huan-Huan Q, Wang X, Fujiyama A, Toyoda A, Ayers K, Blum A, Czech B, Neumuller R, Yan D, Cavallaro A, Hibbard K, Hall D, Cooley L, Hannon GJ, Lehmann R, Parks A, Mohr SE, Ueda R, Kondo S, Ni J-Q, Perrimon N. 2015. The Transgenic RNAi Project at Harvard Medical School: Resources and Validation. *Genetics* **201**:843–852. doi:10.1534/genetics.115.180208

Rodahl LM, Haglund K, Sem-Jacobsen C, Wendler F, Vincent J-P, Lindmo K, Rusten TE, Stenmark H. 2009. Disruption of Vps4 and JNK Function in *Drosophila* Causes Tumour Growth. *PLoS One* **4**:e4354. doi:10.1371/journal.pone.0004354

Shen W, Ganetzky B. 2009. Autophagy promotes synapse development in *Drosophila*. *J Cell Biol* **187**:71–79. doi:10.1083/jcb.200907109

Urban E, Nagarkar-Jaiswal S, Lehner CF, Heidmann SK. 2014. The Cohesin Subunit Rad21 Is Required for Synaptonemal Complex Maintenance, but Not Sister Chromatid Cohesion, during Drosophila Female Meiosis. *PLOS Genetics* **10**:e1004540. doi:10.1371/journal.pgen.1004540

Wagh DA, Rasse TM, Asan E, Hofbauer A, Schwenkert I, Dürrbeck H, Buchner S, Dabauvalle M-C, Schmidt M, Qin G, Wichmann C, Kittel R, Sigrist SJ, Buchner E. 2006. Bruchpilot, a protein with homology to ELKS/CAST, is required for structural integrity and function of synaptic active zones in *Drosophila*. *Neuron* **49**:833–844. doi:10.1016/j.neuron.2006.02.008

Walsh RB, Dresselhaus EC, Becalska AN, Zunitch MJ, Blanchette CR, Scalera AL, Lemos T, Lee SM, Apiki J, Wang S, Isaac B, Yeh A, Koles K, Rodal AA. 2021. Opposing functions for retromer and Rab11 in extracellular vesicle traffic at presynaptic terminals. *J Cell Biol* **220**:e202012034. doi:10.1083/jcb.202012034

Table S3: Genotypes and Statistics by Dataset

Experiments were done at m67 unless otherwise noted
All larvae are male unless otherwise noted
Analysis performed in Volocity unless otherwise noted
Presynaptic volume: α-HRP objects > 7μm^3
Postsynaptic volume: 3μm dilated from presynaptic volume
A: Sum intensity of signal in thresholded objects in presynaptic volume, normalized to presynaptic volume
B: Sum intensity of signal in thresholded objects in postsynaptic volume, normalized to presynaptic volume
ns: not significantly different; SDCM: spinning disc confocal microscopy; TEM: transmission electron microscopy

Figure	Genotype/Conditions	N	Measurement	Statistical Test(s)
1A, E **SDCM**	Gal4^{C380}/Y;; Syt4-GFP/UAS-mcherry-RNAi -VALIUM20 Gal4^{C380}/Y;; Syt4-GFP/UAS-Tsg101-RNAi	8 larvae/ 21 NMJs 8 larvae/ 17 NMJs	Syt4-GFP intensity levels A, B	Pre: Unpaired t-test, p<0.05 Post: Mann-Whitney, p<0.0001
1B, F **SDCM**	Gal4^{Vglutx}/Y; UAS-Evi-GFP/+; UAS-mcherry-RNAi-VALIUM20/+ Gal4^{Vglutx}/Y; UAS-Evi-GFP/+; UAS-Tsg101-RNAi/+	7 larvae/ 21 NMJs 8 larvae/ 25 NMJs	Evi-GFP intensity levels A, B	Pre: Mann-Whitney, p<0.001 Post: Mann-Whitney, p<0.001
1C, D, G, H **SDCM**	Gal4^{Vglutx}/Y; UAS-APP-GFP/+; UAS-mcherry-RNAi-VALIUM20/+ Gal4^{Vglutx}/Y; UAS-APP-GFP/+; UAS-Tsg101-RNAi/+	6 larvae/ 15 NMJs 6 larvae/ 19 NMJs	APP-GFP intensity levels A, B	Pre: Mann-Whitney, p=0.56 ns Post: Unpaired t-test, p<0.05
			Nrg intensity levels A, B	Pre: Mann-Whitney, p=0.31 ns Post: Mann-Whitney, p<0.0001
1I, J **SDCM**	w^{1118} *Hrs*^{D28}/Df(2L)Exel6277	8 larvae/ 24 NMJs 8 larvae/ 26 NMJs	Nrg intensity levels A, B	Pre: Mann-Whitney, p<0.001 Post: Mann-Whitney, p<0.0001
1K-M **SDCM**	Gal4^{C380}/Y; Syt4-GFP/UAS-mcherry-RNAi-VALIUM20 Gal4^{C380}/Y; UAS-Shrub-RNAi/+ ; Syt4-GFP/+	6 larvae/ 22 NMJs 6 larvae/ 18 NMJs	Syt4-GFP intensity levels A, B	Pre: Mann-Whitney, p=0.68 ns Post: Mann-Whitney, p<0.001
			Nrg intensity levels A, B	Pre: Mann-Whitney, p<0.01 Post: Mann-Whitney, p<0.001

1N-P **SDCM**	Gal4^{C380}/Y;; Syt4-GFP/UAS-mcherry-RNAi-VALIUM20 Gal4^{C380}/Y;; UAS-Vps4^{DN}/+ ; Syt4-GFP/+	8 larvae/ 25 NMJs 8 larvae/ 27 NMJs Female	Syt4-GFP intensity levels A, B	Pre: Unpaired t-test, p<0.001 Post: Mann-Whitney, p<0.0001
			Nrg intensity levels A, B	Pre: Mann-Whitney, p<0.0001 Post: Mann-Whitney, p<0.0001
2A, S1A **Airyscan**	Gal4^{Vglutx}/Y; GFP-Rab5-KI/+ Gal4^{Vglutx}/Y; GFP-Rab5-KI/+; UAS-Tsg101-RNAi/+	6 larvae/ 20 NMJs 6 larvae/ 17 NMJs	Mander's coefficients (fraction of Nrg in GFP-Rab5 positive puncta and fraction of GFP-Rab5 in Nrg positive puncta)	M1: Mann-Whitney, p<0.0001 M2: Unpaired t-test, p<0.0001
2A, S1B **Airyscan**	Gal4^{Vglutx}/Y;; YFP-myc-Rab7KI/+ Gal4^{Vglutx}/Y;; YFP-myc-Rab7KI, UAS-Tsg101-RNAi/+	7 larvae/ 20 NMJs 7 larvae/ 17 NMJs	Mander's coefficients (fraction of Nrg in YFP-Rab7 positive puncta and fraction of YFP-Rab7 in Nrg positive puncta)	M1: Mann-Whitney, p<0.01 M2: Unpaired t-test, p<0.01
2A, S1C **Airyscan**	Gal4^{C380}/Y;; Syt4-GFP/UAS-mcherry-RNAi-VALIUM20 Gal4^{C380}/Y;; Syt4GFP/UAS-Tsg101-RNAi	7 larvae/ 25 NMJs 9 larvae/ 25 NMJs	Mander's coefficients (fraction of Syt4-GFP in anti-Rab11 positive puncta and fraction of anti-Rab11 in Syt4-GFP positive puncta)	M1: Unpaired t-test, p<0.0001 M2: Mann-Whitney: p<0.0001
2A, S1D-F Rab11 **Airyscan**	Gal4^{C380}/Y;; Syt4-GFP/UAS-mcherry-RNAi-VALIUM20 Gal4^{C380}/Y;; Syt4GFP/UAS-Tsg101-RNAi	7 larva/ 23 NMJs 9 larva/ 25 NMJs	Rab11 intensity levels A	Unpaired t-test, p<0.001
			Number of anti-Rab11 positive puncta in HRP volume (puncta count/µm^3)	Mann-Whitney, P>0.05 ns
			Average anti-Rab11 puncta size (total Rab11 volume µm^3/puncta number)	Mann-Whitney, p<0.05
2A, S1D-F Rab5 **Airyscan**	Gal4^{Vglutx}/Y; GFP-Rab5-KI/+ Gal4^{Vglutx}/Y; GFP-Rab5-	6 larva/ 20 NMJs 6 larva/ 17 NMJs	GFP-Rab5 intensity levels A	Mann-Whitney, p<0.05

	KI/+; UAS-Tsg101-RNAi/+		Number of GFP-Rab5 positive puncta in HRP volume (puncta count/µm^3)	Unpaired t-test, p<0.05
			Average GFP-Rab5 puncta size (total Rab5 volume µm^3/puncta number)	Unpaired t-test, p<0.001
2A, S1D-F Rab7 **Airyscan**	Gal4^{Vglutx}/Y;; YFP-myc-Rab7KI/+ Gal4^{Vglutx}/Y;; YFP-myc-Rab7KI, UAS-Tsg101-RNAi/+	7 larva/ 20 NMJs 7 larva/ 17 NMJs	YFP-Rab7 intensity levels A	Mann-Whitney, p=0.14 ns
			Number of YFP-Rab7 positive puncta in HRP volume (puncta count/µm^3)	Mann-Whitney, p=0.73 ns
			Average YFP-Rab7 puncta size (total Rab7 volume µm^3/puncta number)	Mann-Whitney, p=0.25 ns
2B **TEM**	Gal4^{Vglutx}/Y;; UAS-mcherry-RNAi- VALIUM20/+ Gal4^{Vglutx}/Y;; UAS-Tsg101RNAi/+	40 boutons from 3 larvae 56 boutons from 3 larvae	Fraction of images with three or more autophagic vacuoles	Fisher's exact test, p<0.0001
2C-E, S2F **Airyscan**	Gal4^{Vglutx}/Y; UAS-GFP-mCherry-Atg8/+; UAS-Luciferase-RNAi-VALIUM10/+ Gal4^{Vglutx}/Y; UAS-GFP-mCherry-Atg8/+; UAS-Tsg101-RNAi/+ Gal4^{Vglutx}/Y; UAS-GFP-mCherry-Atg8/+ Gal4^{Vglutx}/Y; UAS-GFP-mCherry-Atg8, *Hrs*^{D28}/Df(2L)Exel6277	8 larvae each 4 male, 4 female per genotype	(2D-E) Fraction of grouped cell bodies volume occupied by GFP signal or mCherry signal. (S2F) Mander's coefficient for fraction total mCherry signal in GFP-positive volume	GFP in Tsg101: Mann-Whitney, p<0.001 mCherry in Tsg101: Mann- Whitney, p<0.001 GFP in Hrs: Mann-Whitney, p=0.35 ns mCherry in Hrs: Unpaired t-test, p <0.001 Mander's Hrs: Mann-Whitney, p=0.3 ns Mander's Tsg101: Mann-Whitney, p<0.001
2F, G **SDCM**	Gal4^{C380}/Y;; Syt4GFP/UAS-mcherryRNAi-VALIUM20 Gal4^{C380}/Y;; Syt4GFP/UAS-Tsg101RNAi	10 larvae 8 larvae	Intensity measurement from an ROI containing 6-8 cell bodies in ImageJ	Unpaired t-test, p<0.0001

2H, I **SDCM**	Gal4^{C380}/Y;; Syt4GFP/UAS-mcherryRNAi- VALIUM20 Gal4^{C380}/Y;; Syt4GFP/UAS-Tsg101RNAi	10 larvae 9 larvae	Intensity measurement from HRP thresholded axon bundles proximal (within ~100-300µm) to the ventral ganglion in ImageJ	Unpaired t-test, p<0.05
S3A, B **SDCM**	Gal4^{Vglutx}/Y; UAS-AP-PGFP/+; UAS-mcherryRNAi- VALIUM20/+ Gal4^{Vglutx}/Y; UAS-AP-PGFP/+; UAS-Tsg101RNAi/+	12 larvae 12 larvae	Kymograph analysis, manual count of anterograde, retrograde, stationary, and complex moving APP-GFP particles in ImageJ	Unpaired t-test, Stationary: p<0.001 Retrograde: p0.48 ns Anterograde: p=0.50 Complex: p=0.12
S3A, C **SDCM**	Gal4^{Vglutx}/Y; UAS-AP-PGFP/+; UAS-mcherryRNAi- VALIUM20/+ Gal4^{Vglutx}/Y; UAS-AP-PGFP/+; UAS-Tsg101RNAi/+	12 larvae 12 larvae	Kymograph analysis, calculation of the slope of particle tracks, including segments from complex tracks in ImageJ	Retrograde: Mann-Whitney, p<0.05 Anterograde: Unpaired t-test p=0.68 ns
3A, C-E **SDCM**	Gal4^{Vglutx}/Y;; UAS-mcherryRNAi- VALIUM20/+ Gal4^{Vglutx}/Y;; UAS-Tsg101RNAi/+ *evi^{2}/evi^{2}*	7 larvae/14 A2 NMJs, 12 A3 NMJs 7 larvae/11 A2 NMJs, 12 A3 NMJs 7 larvae/8 A2 NMJs, 12 A3 NMJs	(C) Active zone number on muscle 6/7	A2: One-way ANOVA with Tukey's multiple comparison's test, p<0.001 A3: One-way ANOVA with Tukey's multiple comparison's test, p<0.001
			(D) Number of active zones per NMJ area on muscle 6/7	A2: Kruskal-Wallis with Dunn's multiple comparison's test, p<0.001 A3: One-way ANOVA with Tukey's multiple comparison's test, p<0.001
			(E) Number of boutons on muscle 6/7	A2: One-way ANOVA with Tukey's multiple comparisons test, p<0.001 A3: One-way ANOVA with Tukey's multiple comparisons test, p<0.001

3B **SDCM**	Gal4^{Vglutx}/Y;; UAS-mcherryRNAi- VALIUM20/+ Gal4^{Vglutx}/Y;; UAS-Tsg101RNAi/+ *evi^2/evi^2*	26 larvae/ 87 NMJs 26 larvae/ 87 NMJs 29 larvae/ 91 NMJs (Pooled data from 4 independent experiments, mix of males and females)	Fraction of images displaying expanded "feathery" DLG pattern	Fishers exact test WT vs *evi^2* p<0.0001 WT vs Tsg101^{KD} p=0.27
3F-H **SDCM**	Gal4^{C380}/Y;; UAS-mcherryRNAi-VALIUM20/+ Gal4^{C380}/Y;; UAS-Tsg101RNAi/+ Gal4^{C380}/Y; UAS-Shrub-RNAi/+ *evi^2/evi^2*	20°C: 7 larvae/ 24 NMJs, 25°C: 19 larvae/ 63 NMJ 20°C: 7 larvae/ 24 NMJs, 25°C: 19 larvae/ 63 NMJs 20°C: 7 larvae/ 23 NMJs 20°C: 8 larvae/ 24 NMJs, 25°C: 21 larvae/ 67 NMJs All larvae at 20°C were female and all larvae at 25°C were male. 25°C was pooled data across 3 independent experiments.	Ghost bouton number on muscle 6/7 (HRP-positive bouton with no postsynaptic Dlg)	25°C: A2: Kruskal-Wallis test with Dunn's multiple comparison's test, p,0.001 25°C: A3: Kruskal-Wallis test with Dunn's multiple comparison's test, p<0.05. 20°C: A2: Kruskal-Wallis test with Dunn's multiple comparison's test, p,0.001 20°C: A3: Kruskal-Wallis test with Dunn's multiple comparison's test, p,0.001
4A, B **SDCM**	Gal4^{C380}/Y;; Syt4GFP/UAS-mcherry-RNAi-VALIUM20 Gal4^{C380}/Y;; Syt4-GFP/UAS-Tsg101RNAi	WT Mock: 6 larvae/ 22 NMJs WT Stim: 5 larvae/ 23 NMJs Tsg101 Mock: 6 larvae/ 25 NMJs Tsg101 Stim: 5 larvae/ 23 NMJs	Ghost bouton number on muscle 4 (HRP-positive bouton with no postsynaptic Dlg)	WT stim vs mock: Mann-Whitney, p<0.001 Tsg101 stim vs mock: Mann-Whitney, p<0.001 WT stim vs Tsg101 stim: Mann-Whitney, p=0.81 ns
4C, D **electro-physiology**	Gal4^{Vglutx}/+;; UAS-mcherry-RNAi- VALIUM20/+ Gal4^{Vglutx}/+;; UAS-Tsg101-RNAi/+	9 larvae / 12 NMJs 8 larvae / 12 NMJs	Fold change in mEJP frequency	NA

4F, H **SDCM**	Gal4^{C380}/Y; Syt4-GFP Gal4^{C380}/Y; UAS-DegradGFP, Syt4-GFP	29 NMJ branches 25 NMJ branches	Syt4-GFP intensity levels A, B	Pre: Unpaired t-test, p<0.001 Post: Unpaired t-test, p<0.001
4G, I **SDCM**	Syt4-GFP UAS-DegradGFP; Gal4^{C57}, Syt4-GFP	8 larvae/ 33 NMJ branches 8 larvae/ 30 NMJ branches	Syt4-GFP intensity levels A, B	Pre: Mann-Whitney, p=0.59 ns Post: Mann-Whitney, p=0.56 ns
4J (F, G) **SDCM**	Genotypes from 4F and 4G	N from 4F and 4G	Number of Syt4-GFP positive puncta in HRP volume (puncta count/µm^3)	C380: Unpaired t-test, p<0.001 C57: Mann-Whitney, p=0.84 ns
S2A **SDCM**	Gal4^{Vglutx}/Y; UAS-GFP-mCherry-Atg8/+; UAS-Luciferase-RNAi-VALIUM10/+ Gal4^{Vglutx}/Y; UAS-GFP-mCherry-Atg8/+; UAS-Atg1-RNAi/+	2 larvae 3 larvae	No measurements	NA
S2B, C **SDCM**	Gal4^{Vglutx}/Y;; UAS-mcherry-RNAi- VALIUM20/+ Gal4^{Vglutx}/Y;; UAS-Atg1-RNAi/+	8 larvae/ 30 NMJs 8 larvae/ 22 NMJs	Nrg intensity levels A, B	Pre: Unpaired t-test, p<0.01 Post: Mann-Whitney, p<0.05
S2D, E **SDCM**	w^{1118} *Atg2*^{EP3697}/Df(3L)Exel6091	8 larvae/ 18 NMJs 7 larvae/ 17 NMJs Mixed males and females	Nrg intensity levels A, B	Pre: Mann-Whitney, p<0.01 Post: Unpaired t-test, p<0.001
S3D-F **SDCM**	Gal4^{Vglutx}/Y; UAS-Mito-GFP/+; UAS-mcherry-RNAi- VALIUM20/+ Gal4^{Vglutx}/Y; UAS-Mito-GFP/+; UAS-Tsg101-RNAi/+	11 larvae 11 larvae	Kymograph analysis, manual count of percentage of anterograde and retrograde mito-GFP particles in ImageJ	Retrograde: Unpaired t-test, p=0.70 ns Anterograde: Unpaired t-test, p=0.70 ns
			Kymograph analysis, calculation of the slope of particle tracks in ImageJ	Retrograde: Unpaired t-test, p=0.65 ns Anterograde: Unpaired t-test, p=0.36 ns
S3G, H **SDCM**	Gal4^{Vglutx}/Y; UAS-Mito-GFP/+; UAS-mcherry-RNAi-VALIUM20/+ Gal4^{Vglutx}/Y; UAS-Mito-	11 larvae 11 larvae	Intensity measurement from first frame of videos of axon bundles proximal (within ~100-	Unpaired t-test, p=0.79 ns

	GFP/+; UAS-Tsg101-RNAi/+		300µm) to the ventral ganglion in ImageJ	
S4C, D **SDCM**	Gal4^{Vglutx}/+;; UAS-mcherry-RNAi- VALIUM20/+ Gal4^{Vglutx}/+;; UAS-Tsg101-RNAi/+	7 larvae / 13 NMJs 7 larvae / 13 NMJs	Ghost bouton number on muscle 6/7 (HRP-positive bouton with no postsynaptic Dlg)	Unpaired t-test, p=0.65 ns
S4B **SDCM**	Gal4^{C380}/Y or w;; Syt4^{TSTEP} Gal4^{C380}/Y or w;; Syt4 ^{TSTEP}/UAS-Rippase, Syt4^{TSTEP} w;; Gal4^{C57}, Syt4 ^{TSTEP}/UAS-Rippase, Syt4^{TSTEP}	No quantification	No measurements	NA
S4E **SDCM**	Dlg1-MiMIC/+; CyOGFP/+; Gal4^{C57}, Syt4-GFP/TM6 Dlg1-MiMIC/+; UAS-DegradGFP/+; Gal4^{C57}, Syt4-GFP/ Gal4^{C57}	4 larvae/ 14 NMJs 4 larvae/ 13 NMJs	No measurements	NA